Fusion Reactions

1 General Considerations

The fusion of two nuclei to form a heavier compound nucleon, in a very important reaction. Besides its a way to produce nuclei with very high spins and accordingly to study the rapid rotation phenomena of nuclei. At very low energies nuclear fusion is of paramount importance for stellar energy production and nuclear synthesis as originally proposed by H. Bethe [1]. Further, they are very sensitive to nuclear structure when measured below-the-Coulomb-barrier energies (to be explained in what follows).

We shall emphasize the fusion of halo nuclei, where break up effects are important and also the production, through fusion, of other type of exotic nuclei, the super heavy element (SHE). As a background to both subjects, we present below a detailed account of a simple picture of the fusion reactions namely, the tunneling through a local one-dimensional real potential barrier formed from the addition of an attractive nuclear and a repulsive Coulomb potentials. We further assume that absorption into the fusion channels (compound nucleon) ensues in the inside region to the left of the barrier after the tunneling through the barrier (from the right) has occurred.

The one-dimensional potential for the $\ell + 1$ partial wave is wave

$$V_\ell(r) = V_N(r) + V_c(r) + \frac{\hbar^2 \ell(\ell+1)}{2\mu r^2} \tag{1}$$

where $V_N(r)$ is the attractive nuclear potential takes to be e.g. of a Woods-Saxon form

$$V_N(r) = \frac{-V_o}{1 + \exp\left[(R - R_0)/a\right]}, \tag{2}$$

$V_c(r)$ is the Coulomb potential given by

$$V_c(r) = \begin{cases} Z_1 Z_2 \mathrm{e}^2/r & r \geq R_c \\ Z_1 Z_2 \mathrm{e}^2/2R_c \left[3 - (r/R_c)^2\right] & r \leq R_c \end{cases} \tag{3}$$

and the centrifugal potential is given as usual by $\hbar^2 \ell(\ell+1)/2\mu r^2$:

In figure 1(a) we show the effective potentials for $^{64}Ni + ^{64}Ni$ for three values of ℓ. The Coulomb barrier (peak) is clearly seen in the lowest two curves and it becomes less conspicuous for $\ell = 150$ as the centrifugal repulsion starts dominating. If the c.m. energy is 160 MeV, then all partial wave up to about $\ell = 100$ will contribute. In the region below $\ell = 95$ the tunneling probability is 1, for $\ell > 160$ it is zero. Then one expects a form for this tunneling probability (fusion transmission coefficient) to be close to a Fermi function (being unity for small ℓ and going gradually to zero at larger ℓ values).

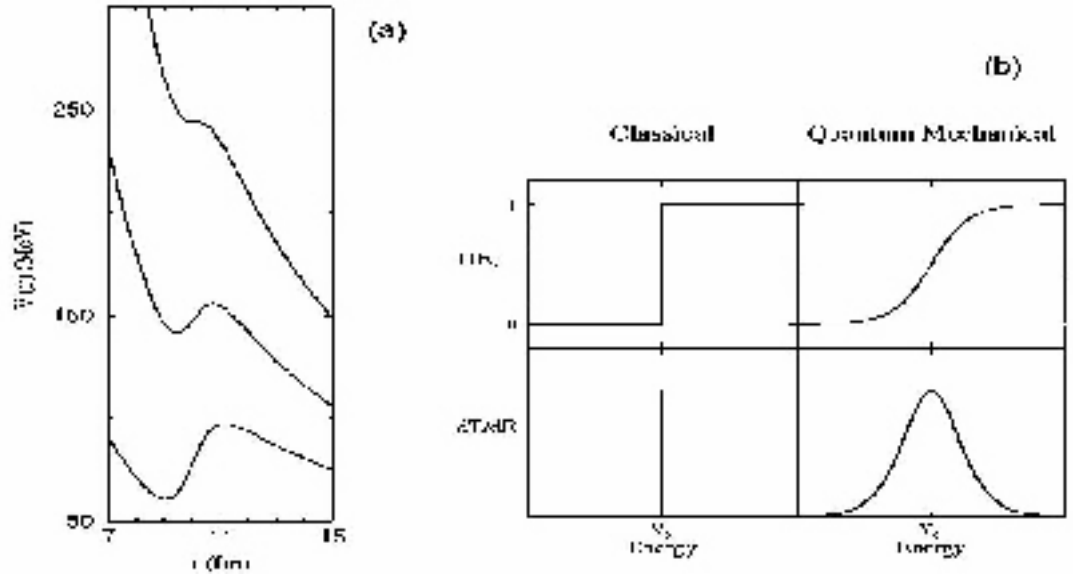

Figure 1 (a) One dimensional potential of Eq. 1 for the ^{64}Ni+^{64}Ni system for serveral ℓ values. The lowest barrier is for $\ell = 0$ (the bare barrier). The middle and top barriers are for $\ell = 100$ and $\ell = 150$, respectively. (b) Classical (on the left) and quantum-mechanical (on the right) transmission probabilities for a one-dimensional potential barrier.

The fusion cross-section is just the sum of all the T_ℓ is weighted with the factor $2\ell + 1$, i.e.,

$$\sigma_F(E) = \frac{\pi^\ell}{k^2} \sum_{\ell=0}^{\infty} (2\ell + 1) T_\ell(E) = \sum_{\ell=0}^{\infty} \sigma_F(\ell, E) \tag{4}$$

where $\sigma_F(\ell, E)$ is the partial fusion cross-section.

The calculation of $T_\ell(E)$ must rely on solving the appropriate Schrödinger equation with incoming wave boundary condition (IWBC). Here IWBC enforces the condition that one the system is in the pocket, it does not return An alternative approximate way of calculating T_ℓ is through the use of the semiclassical approximation [2]

$$T_\ell E = \{1 + \exp\} [2S_\ell(E)]^{-1}, \tag{5}$$

where the WKB integral $S_\ell(E)$ is given by

$$S_\ell(E) = \sqrt{\frac{2\mu}{\hbar^2}} \int_{r_1(\ell)}^{r_2(\ell)} dr \left[V_o(r) + \frac{\hbar^2 (\ell + 1/2)^2}{2\mu r^2} - E \right]^{\frac{1}{2}} \tag{6}$$

here $r_1(\ell)$ and $r_2(\ell)$ are the outermost classical turning points determined by setting

$$V_o + \frac{\hbar^2 (\ell + 1/2)^2}{2\mu r^2(\ell)} = E \tag{7}$$

The "width" of the barrier is just $r_2(\ell) - r_1(\ell)$.

For energies that correspond to a trajectory close, but below, the top of the barrier, the barrier looks like an inverted parabola. Then one expands $V_N + V_c \equiv V_o(r)$

$$V_o(r) = V_B - \frac{1}{2}\mu^2\omega^2 (r - R_B)^2 \tag{8}$$

A more precise statement concerning Eq. 8 should involve the centrifugal potential. However the inclusion of this latter potential only changes V_{Bo} to $V_{B\ell} \equiv V_{Bo} + \hbar^2 \left(\ell + \frac{1}{2}\right)^2 / 2\mu R_B^2$. The change in the curvature of the barrier, measured by ω, is very small and is thus neglected.

With the parabolic approximation for $V_o + \hbar^2 (\ell + 1/2) / 2\mu r^2 = V_{B\ell} - \frac{1}{2}\mu\omega^2 (r - R_B^2)^2$, the integral $S_\ell(E)$ can be performed straight forwardly and when inserted in T_ℓ, gives the well-known Hill-Wherler formula

$$T_\ell = \frac{1}{1 + \exp 2\pi (V_{B\ell} - E) / \hbar\omega}, \tag{9}$$

with

$$V_{B\ell} = V_{Bo} + \frac{\hbar^2 (\ell + 1/2)^2}{2\mu R_B^2} \tag{10}$$

The above Hill-Wherler expression for T_ℓ, Eq. 9, is valid only in the proximity of the barrier (E slightly above and slightly below $V_{B\ell}$). For energies that do not satisfy this condition the parabolic approximation is a bad one. One has to evaluate $S_\ell(E)$ exactly.

With the form of $T_\ell(E)$ determined (at least in the vicinity of the height of the Coulomb barrier), one can now evaluate the fusion cross-section

$$\sigma_F(E) = \frac{\pi}{k^2} \sum_{\ell=0} (2\ell + 1) \frac{1}{1 + \exp\left[V_{Bo} + \hbar^2 (\ell + 1/2)^2 / 2\mu R_B^2 - E\right]} \tag{11}$$

Since many partial waves contribute to the sum, one may replace the sum by an integral. Call $(\ell + 1/2)^2 = \chi$, and write

$$\sigma_F(E) = \frac{2\pi}{k^2} \int_{1/4}^{\chi} d\chi \frac{1}{1 + \exp\left[(V_{Bo} - E) + \hbar^2\chi / 2\mu R_B^2\right]} \tag{12}$$

The integral yields

$$\sigma_F(E) = \frac{\hbar\omega R_B^2}{2E} \ell n \left[1 + \exp\left[\frac{2\pi}{\hbar\omega} (E - V_{Bo})\right]\right] \tag{13}$$

The above expression for $\sigma_F(E)$ is referred to as the Wong formula [3]. At high energies, $E \gg V_{Bo}$, the exponential dominates over unity and one finds the geometrical for $\sigma_F(E)$

$$\sigma_F(E) = \pi R_B^2 \left(1 - \frac{V_{Bo}}{E}\right) \tag{14}$$

The above form can also be obtained in the classical limit where $T_\ell(E)$ is a step function and accordingly by using $\omega = 0$.

Before we concentrate our discussion on σ_F at sub-barrier energies, we indulge a bit on fusion at energies above the barrier. Here it is seen that after an initial rise, $\sigma_F(E)$ then reaches a maximum followed by drop. The drop in $\sigma_F(E)$ is attributed to the competing deep inelastic processes. To account for such a structure in σ_F, one can multiply T_ℓ by the fusion probability [4]. Thus T_ℓ takes into account the tunneling into the strong absorption radius, R_{sa}, which is situated slightly to the left of the barrier. Part of the flux that reaches R_{sa} would fuse while the other part is lost to deep inelastic processes.

Accordingly

$$\sigma_F(E) = \frac{\pi}{k^2}\sum_{\ell=0}^{\infty}(2\ell+1)\,T_\ell(E)\,P_\ell^{(F)}(E) \tag{15}$$

Since $T_\ell(E)$ contains reference to the barrier radius R_{Bo} only, $P_\ell^{(F)}(E)$ must contain reference to $R_{sa} \equiv R_{critical} = R_c$. The sum over ℓ now extends to $\ell_c(R_c)$, the critical angular momentum associated with R_c.

The calculation of $\sigma_F(E)$ using the integral form, Eq. 12, with an upper limit in the integral $\chi_c \equiv (\ell_c + 1/2)^2$, can be done easily and one obtains the Glas-Mosel formula [4]

$$\sigma_F = \frac{\hbar\omega R_B^2}{2E}\ell n\left\{1+\exp\left[\frac{2\pi}{\hbar\omega}(V_{Bo}-E)\right]\right. \tag{16}$$

$$\left.\times\left[\exp\left[-\frac{2\pi}{\hbar\omega}\left(\frac{\hbar^2(\ell_c+1/2)^2}{2\mu R_c^2}\right)\right]+\exp\left[\frac{2\pi}{\hbar\omega}(V_{Bo}-E)\right]\right]^{-1}\right\} \tag{17}$$

Calling $E - V_{Bo} = \hbar^2\left(\ell_B + \frac{1}{2}\right)^2/2\mu R_B^2$, the above expression can be reduced further into

$$\sigma_F = \frac{\hbar\omega R_B^2}{2E}\ell n\left\{\frac{\exp(\alpha\ell_B^2)+1}{\exp(\alpha(\ell_B^2-\ell_c^2))+1}\right\}, \tag{18}$$

$$\alpha \equiv \frac{2\pi}{\hbar\omega}\frac{\hbar^2}{2\mu R_B^2} \tag{19}$$

Clearly, if σ_F of Eq. 13 is considered very close to the total reaction cross-section, since peripheral processes have much smaller cross-sections than σ_F at lower enegies, Eq. 18, shows clearly that $\sigma_F < \sigma_R$. It has become common to call the region where $\sigma_F \sim \sigma_R$ as Region I while that where $\sigma_F < \sigma_R$ as Region II. In this latter region, deep inelastic collisions DIC (where a large amount of relative energy is converted into internal excitation of the two fragments) constitute a considerable part of σ_R. Figure **??**(a) shows the data of systems exhibiting Regions I and II.

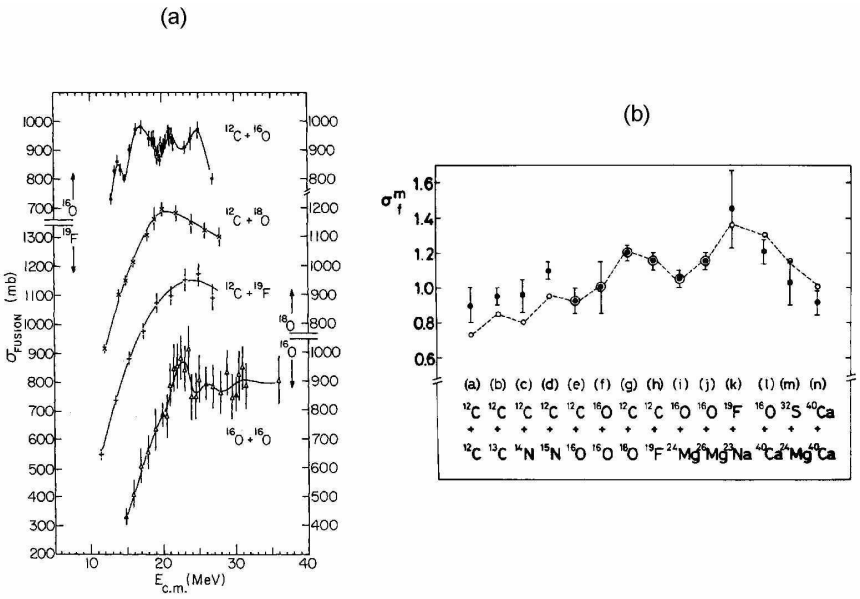

Figure 2 (a) Fusion data for several systems exhibiting regions I and II. See text for details. (b) The maximum values of σ_F (in barns) for several systems. The theoretical calculation are within the statistical yrast line model of reference 8.

A possible physical interpretation for ℓ_{cr}, besides the one related to the competition between fusion and DIC, may reside in the compound nucleus formed in the process. The *yrast line model* states that the angular momentum imparted to the compound nucleus (CN) can be associated with the yrast line which is the maximum angular momentum for a given excitation energy. Since the excitation energy of the CN is $E_{c.m.} + Q$ where Q is the Q-value of the fusion $A_1 + A_2 \rightarrow (A_1 + A_2)$, then the yrast line is

$$E_{c.m.} + Q = \frac{\hbar^2 J_y \left(J_y + 1\right)}{2\Im} \tag{20}$$

where $\Im$ is the moment of inertia of the CN. For a rigid spherical body, $\Im = 2MR_{CM}^2/5$.

Then

$$J_y^2 = \frac{2\Im E_{c.m.}}{\hbar^2}\left(1 + \frac{Q}{E_{c.m.}}\right) \tag{21}$$

One then makes the identification $\ell_{cr} = J_y.$ at high energies,

$$\sigma_F \simeq \frac{\pi\hbar^2}{2\mu E_{c.m.}}\ell_{cr}^2 = \frac{\pi^2\Im}{\mu}\left(1 + \frac{Q}{E_{c.m.}}\right) \tag{22}$$

A variance of the CN model is the statistical Yrast Line Model of Lee at al. [5], which says that part of the excitation energy $E_{c.m.} + Q$ is statistical (thermal) in

nature. Calling this energy ΔQ one has

$$\frac{\hbar^2 J'_y \left(J'_y + 1\right)}{2\Im} + \Delta Q = E_{c.m.} + Q \tag{23}$$

and thus

$$\sigma_F = \frac{\pi\Im}{\mu}\left(1 + \frac{Q - \Delta Q}{E_{c.m.}}\right) \tag{24}$$

The above expression can account for a wide range of experimental data if $\Delta Q = 10MeV$ and $r_o = 1.2fm$, where r_o is the radius parameter that enters in the calculation of the moment of inertia $\Im$. An example of how the above formula works is shown in Figure **??**(b) which exhibits the maximum value of σ_F as a function of the system (Q-value), obtained with $\Delta Q = 5\,MeV$.

2 Sub-Barrier Fusion

At energies close or below the $\ell = 0$ barrier (the Coulomb barrier), the collision time become longer and specific effects of the structure of the participating nuclei in the fusion process become important. In such cases the one-dimensional barrier penetration model does not work anymore and one has to resort to coupled channels treatments. A case which illustrates this effect is supplied by the fusion of only ^{16}O with the well deformed ^{154}Sm target [6]. Here, since the rotational band is well formed in ^{154}Sm, one may freeze the rotation axis and perform a one-dimensional calculation of the type described before. An average over all orientations would then supply σ_F,

$$\sigma_F\left(E_{c.m.}\right) = \int d\Omega\ \sigma_F\left(E_{c.m.}, \Omega\right) \tag{25}$$

where Ω represents the solid angle that describes the direction of the rotation axis of the assumed rigid rotor ^{154}Sm.

One can easily convince oneself that the "equivalent sphere" σ_F of Eq. 24, is larger than σ_F calculated for a spherical ^{154}Sm. The sub-barrier enhancement of σ_F is found to occur in many systems. The calculation of σ_F according to Eq. 24 assumes an infinite moment of inertia of the rotor (degenerate or sudden limit). A more realistic way of calculating σ_F which takes into account the energy loss (Q-value) must rely on coupled channels theory.

Another simple model that can be evaluated analytically is that of a two-level system. Ignoring the angular momentum of the excited state, and its excitation energy one has the two-coupled equations

$$\begin{aligned}
\left(E - \left(-\frac{\hbar^2}{2\mu}\frac{d^2}{dr^2} + V_{(r)}\right)\right)\Psi_1 &= F_{12}\,\Psi_2 \\
\left(E - \left(-\frac{\hbar^2}{2\mu}\frac{d^2}{dr^2} + V_{(r)}\right)\right)\Psi_2 &= F_{21}\,\Psi_2
\end{aligned} \tag{26}$$

If the coupling $F_{12} = F_{21} = F$ is taken to be constant, one can solve for σ_F, by diagonalizing the above two equations

$$\sigma_F = \frac{1}{2}\left(\sigma_F\left(V_B + F\right) + \sigma_F\left(B_B - F\right)\right) \ , \tag{27}$$

which is always large than $\sigma_F\left(V_B\right)$. The inclusion of the non-zero excitation energy can be done without great difficulty. The result of diagonalization gives for σ_F the following

$$\sigma_F = A_+ \ \sigma_+ + A_- \ \sigma_- \tag{28}$$

where

$$\begin{aligned} A_\pm &= \frac{2F^2}{4F^2 + Q^2 \mp Q\sqrt{4F^2 + Q^2}} \\ \sigma_\pm &= \sigma_F\left(V + \lambda_\pm\right) \\ \lambda_\pm &= \frac{1}{2}\left(-Q \pm \sqrt{Q^2 + 4F^2}\right) \end{aligned} \tag{29}$$

when $Q = 0$, one recovers Eq. 27.

The above results can be extended to several channels. One introduces the eigen channels $|C\rangle$ that diagonalize the many-channels Schrödinger equation. The eigen values are denoted by λ_c. Then

$$\sigma_F = \sum_C \left|\langle C|0\rangle\right|^2 \ T_C\left(E, V + \lambda_c\right) \tag{30}$$

where $|0\rangle$ is the entrance channel. For more details on sub-barrier enhancement of fusion see, e.g., Ref. [7].

An interesting observation was made in Ref.. [8] and later elaborated upon in Ref. [9] concerning the extraction of the barrier or eigen barriers directly from the data . It can be seen from the form of T_ℓ given by Hill-Wheeler, Eq. 9, that $T_\ell\left(E\right)$ may be written as $T_o\left(E - \ell\ell + 1)\hbar^2/2\mu \ R^2\right)$. Therefore it is not surprising that the approximation $T_\ell\left(E\right) \simeq T_o\left(E\right) - \ell\left(\ell + 1\hbar^2\right)/2\mu \ R^2\left(E\right)$, with $R\left(E\right)$ being a slowly varying function of E, may tunr out to be reasonably accurate. Then, with $\lambda \equiv \ell + 1/2 \cong \sqrt{\ell\left(\ell + 1\right)}$ and $E \equiv E - \lambda^2/2\mu \ R^2\left(E\right)$

$$\begin{aligned} \sigma_F &= \frac{\pi}{k^2}\sum_{\ell=0}^{\infty}\left(2\ell + 1\right)T_\ell\left(E\right) \simeq \frac{2\pi}{k^2}\int_0^\infty \lambda \ d\lambda \ T\left(\lambda; E\right) \\ &= \frac{\pi R^2\left(E\right)}{E}\int_{-\infty}^{E} dE\prime \ T_o\left(E\prime\right). \end{aligned} \tag{31}$$

Therefore the second derivative $d^2\left(E \ \sigma_F\left(E\right)\right)/dE^2$ can be directly related to the first derivative $dT_o\left(E\right)/dE$, up to corrections coming from the energy dependence

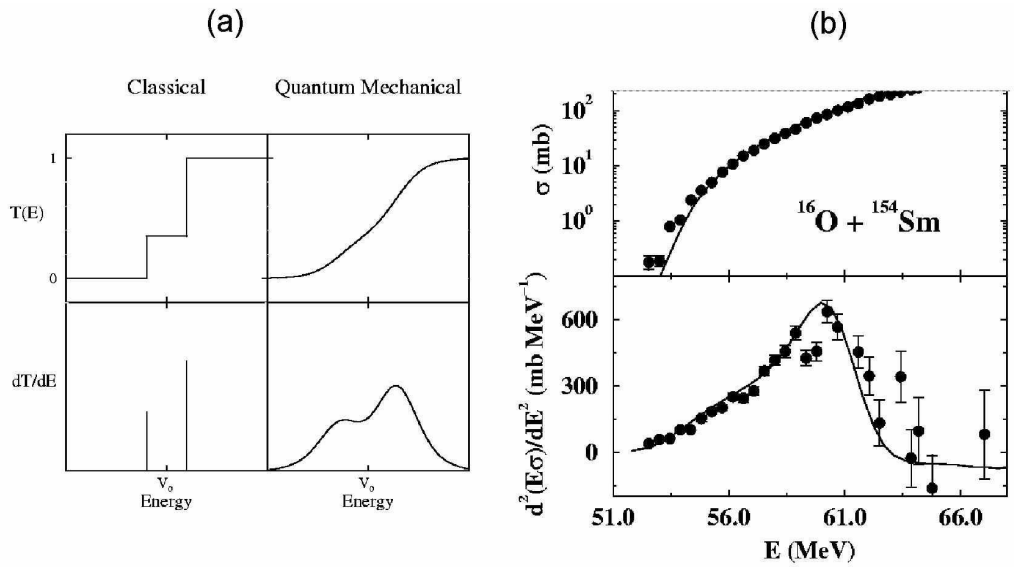

Figure 3 (a) Classical (on the left) and quantum-mechanical (on the right) transmission probabilities for a two-channel coupling. V_0 is the height of the one-dimensional potential barrier coupled to these channels. (b) Fusion cross section and barrier distribution for the ^{16}O+^{154}Sm system by Leiht et al. [11].

of $R\left(E\right)$

$$\frac{d\,T_o\left(E\right)}{dE} \sim \frac{1}{\pi R^2\left(E\right)} \frac{d^2}{dE^2}\left[E\sigma_F\left(E\right)\right] + \Theta\left(\frac{dR}{dE}\right) \tag{32}$$

In figure 3(a) we show an example of dT_o/dE for the one-dimensional and the two-channel barrier tunneling problem. The actual data, e.g. $^{16}O + ^{154}\,Sm$, show a clear deviation from the one-dimensional case whendT/dE is examined, fig. 3(b).

Contrary to the sub-barrier fusion enhancement found in light heavy systems, the fusion of very heavy systems of the type employed in the production of superheavy elements (SHE), shows hindrance when compared to the simple one-dimensional barrier penetration model. The incident energy has to be much higher than the fusion barrier which accounts for fusion of lighter systems, in order for heavy element production to proceed. One needs an "*extra push*", as proposed by Bjornholm and Swiatechi [10]. This extra energy needed for fusion to occur comes about from the fact that the fission barrier for massive systems is located inside the potential barrier in the entrance channel. Ref. [10] (BS) introduced the "extra push" concept; the energy needed to overcome the saddle point in the potential energy surface under the constraint of mass asymmetry, and the "*extra extra push*" which is the energy needed to carry the system beyond (inside) the fission saddle point.

3 Fusion of Halo Nuclei

We have seen that at near or at sub-barrier energies the fusion cross section for stable nuclei exhibits enhancement when compared to the one-dimensional barrier penetration model. Here we extend the discussion to neutron-rich and proton-rich nuclei. As has been already emphasized, the case of halo nuclei is one that observes a special attention. In these loosely bound systems, one has two competing effects. The presence of the halo, namely an extended matter density, tends to lower the Coulomb barrier then enhances the sub-barrier fusion. On the other hand the low Q-value for break-up implies a strong coupling to this channel, which by its nature, would result in a reduction of sub-barrier fusion. In the following we give an account of the work done on these systems and mention the scarce available data. In cases where the halo nucleus has a bound existed state, the enhancement should increase. The overall effect on σ_F can only be assessed with a complete coupled channels calculation. A way of discussing fusion of loosely bound systems subject to break-up is a coupled channel model involving, at least, the entrance channel and the break-up channel. The break-up channel here involves elastic break-up only, since inelastic break-up is a flux that is difficult to recover in a dynamic polarization framework.

The recent availability of radioactive beams has made possible to study fusion reaction reactions involving unstable nuclei. Such reactions are important in processes of astrophysical interest, as well as in the search for superheavy elements. The main new ingredient in fusion reactions induced by unstable projectiles is the strong influence of the breakup channel. In the case of not too unstable projectiles, the effect of this channel in the fusion cross section at low energies is, as in the case of stable beams, to enhance it. At high energies, however, the situation is qualitatively different from the case where only stable nuclei are involved. The contribution from the breakup channel to the fusion reaction is strongly influenced by the low probability that all fragments are captured. Thus, in this case, the fusion cross section is partitioned into a complete and one or more incomplete fusion contributions [12].

The introduction of the breakup channel into a coupled channels calculation is by no means trivial. The difficulty lies in the fact that this channel lies in the continuum, and involves at least, three body system. This problem has been addressed by several authors, using different approaches. Several recent experiments involving fusion of neutron rich ^{6}He and proton rich ^{17}F with heavy targets have been performed with the purpose of exploring these theoretical proposals [13, 14, 15]. All of these measurments, however, exihibit data for the summed fusion plus incomplete fusion cross sections. As, such, the theoretical models proposed for complete fusion can not be presently tested in comparison with the data. To get an idea of the type of data now available,we exhibit in figures 4(a and b), and 5(a) the results obtained in Refs. [13], [14] and [15] for the systems^{6}He ^{238}U, ^{6}He+^{209}Bi and ^{17}F+^{208}Pb, respectively.

In Refs. [12, 16, 17, 18, 19], the coupled-channel problem is simplified by the introduction of the polarization potentials arising from the coupling with the breakup channel [20, 21]. In Refs. [22, 23, 24], the coupled-channel problem is solved directly

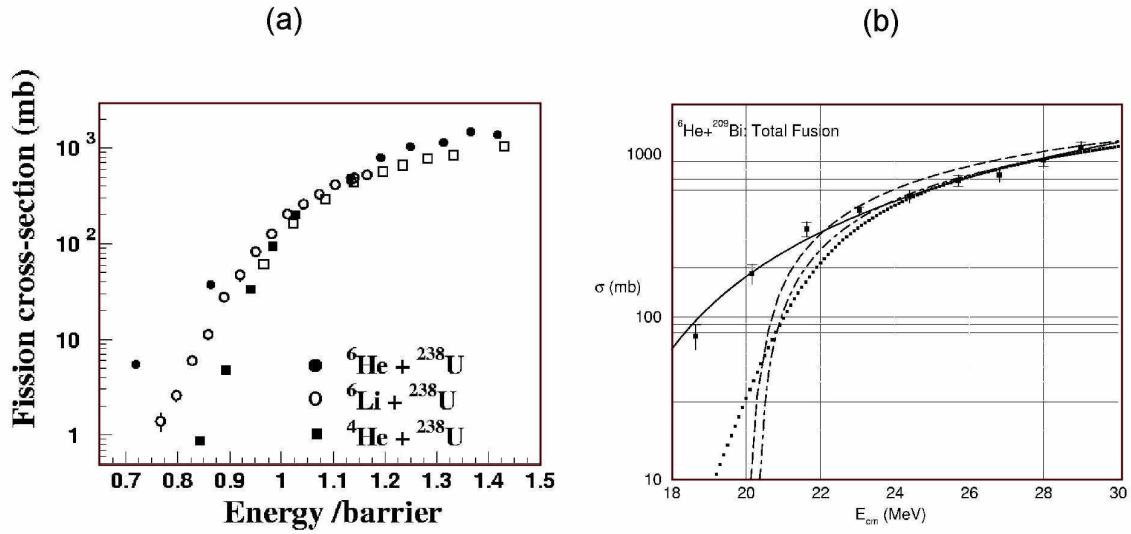

Figure 4 (a) Fusion plus incomplete fusion cross section for the system ^{6}He+^{238}U from reference [13]. (b) Same as figure 7 for the system ^{6}He+^{209}Bi from reference [14].

within different approximation, ranging from the schematic model of Ref. [22] to the huge numerical calculation Ref. [24], performed through continuum discretization.

The polarization potential approach of Refs. [12, 16, 17, 18, 19] has the advantage of leading to simple expressions, which can easily be used in data analysis[25]. However, it employs several approximations which were not thoroughly tested. These approximations can be grouped in two cathegories. In the first are those used in the derivation of the polarization potentials. In the second are the semiclassical approximations for fusion and breakup coefficients, used in calculations of the cross sections. These coefficients are written in terms of barrier penetration factors and survival probabilities, which are evaluated within the WKB approximation.

In the next section we ascertain the quality of the approximations for the transmission coefficients. Approximations in the derivation of the polarization potential will be also be presented. For our purposes, we consider a case where a complete quantum mechanical calculation is feasible and compare exact and approximated cross sections. We study the ^{11}Li + ^{12}C collision, using typical optical and polarization potentials. For simplicity, our polarization potential has no angular momentum or energy dependence and the range is given by the ^{11}Li breakup threshold energy. The strength is consistent with that found in Ref. [20] for the most relevant partial waves in near-barrier fusion.

4 Coupled channel equations and polarization potentials

In a standard coupled channels calculation, the system is described through the distance between centers of projectile and target, $\mathbf{r}$, and a set of intrinsic coordinates,

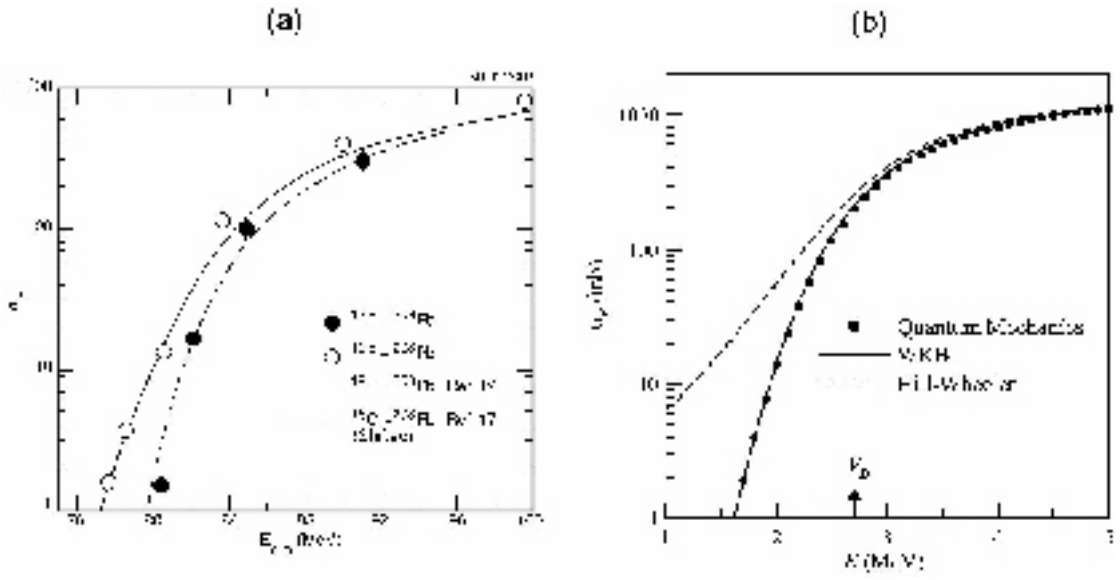

Figure 5 (a) Fusion cross section for the ^{17}F+^{208}Pb system from reference [15]. (b) Hill-Wheeler and WKB approximations to the fusion cross section. The vertical arrow indicates the position of the Coulomb barrier. See text for further details.

ξ, that describe the internal degrees of freedom of one of the nuclei, *e.g.* the target. These coordinates are associated to an intrinsic Hamiltonian h and its eigenfunction set,

$$h\phi_\alpha(\xi) = \epsilon_\alpha \phi_\alpha(\xi)\,, \tag{33}$$

where

$$\int \phi^*_\alpha(\xi)\phi_\beta(\xi)d\xi = \delta_{\alpha,\beta}\,. \tag{34}$$

The system Hamiltonian may then be written as

$$H = T + U^{opt} + h + v(\mathbf{r},\xi)\,. \tag{35}$$

Above, T is the kinetic energy of the relative motion, U^{opt} is the optical potential and $v(\mathbf{r},\xi)$ is the interaction coupling intrinsic and collision degrees of freedom. The optical potential, which is diagonal in channel space, accounts for the average interaction between projectile and target.

Usually the solution of Schrödinger's equation

$$H\Psi(\mathbf{r},\xi) = E\,\Psi(\mathbf{r},\xi)\,, \tag{36}$$

where E is the collision energy in the center of mass frame, is expanded as

$$\Psi(\mathbf{r},\xi) = \sum_\alpha \psi_\alpha(\mathbf{r})\phi_\alpha(\xi)\,, \tag{37}$$

where $\psi_\alpha(\mathbf{r})$ describes the relative motion in channel α. Substituting this expansion in Eq. (36) we obtain the coupled channels equations (see e.g. Ref. [26]),

$$(E_\alpha - H_\alpha)\,\psi_\alpha(\mathbf{r}) = \sum_\beta \mathcal{V}_{\alpha\beta}(\mathbf{r})\,\psi_\beta(\mathbf{r})\,. \tag{38}$$

Above, $E_\alpha = E - \epsilon_\alpha$ and $H_\alpha = T + U_\alpha^{opt}(r)$, where

$$U_\alpha^{opt} \equiv V_\alpha^{opt} - i\,W_\alpha^{opt} \tag{39}$$

is the optical potential in channel α. The imaginary parts have the purpose of accounting for the flux lost to channels neglected in the expansion of Eq.(37). The channel coupling potentials, in Eq.(38) are given by

$$\mathcal{V}_{\alpha\beta}(\mathbf{r}) = \int d\xi\,\phi_\alpha^*(\xi)\,v(\mathbf{r},\xi)\,\phi_\beta(\xi)\,. \tag{40}$$

A consequence of the non-Hermitian nature of H (see Eq.(39)) is that the continuity equation breaks down. This can be checked following the usual procedure to derive the continuity equation. For each α, we evaluate $\psi_\alpha^*(\mathbf{r}) \times$ [Eq.(38)] $-$ [Eq.(38)]$^* \times \psi_\alpha(\mathbf{r})$ and then sum the results. Assuming that $\mathcal{V}_{\alpha\beta}$ is hermitian, we obtain

$$\nabla \cdot \sum_\alpha \mathbf{j}_\alpha = \frac{2}{\hbar}\sum_\alpha W_\alpha^{opt}(\mathbf{r})\,|\psi_\alpha(\mathbf{r})|^2 \neq 0$$

Integrating the above equation inside a large sphere with radius larger than the interaction range and using the definition of the absorption cross section, we obtain the useful relation[27]

$$\sigma_a = \frac{k}{E}\sum_\alpha \langle\psi_\alpha|\,W_\alpha\|\psi_\alpha\rangle\,. \tag{41}$$

4.1 Polarization potentials

In some coupled channel problems, it occurs that one is only interested in the elastic wave function. One example is the study of complete fusion in collisions involving nuclei far from stability, where the breakup threshold is very low. An extreme example is ^{11}Li, which has no bound excited state. In such cases, the coupled channel problem involves only the elastic and the breakup channels. Since the breakup channels contain at least three fragments, their contribution to complete fusion is expected to be negligible. Therefore, only the elastic wave function is required for the calculation of the complete fusion and breakup cross sections.

In such cases, the *polarization potential* approach becomes very convenient. It consists of replacing the coupled channel equations by a single Schrödinger equation for the elastic state. This equation contains a *polarization* term, U^{pol}, added to the optical potential and its solution is identical to the elastic wave function obtained from the coupled channel equations. According to Feshbach [28], the polarization potential

is obtained through elimination of the coupled channel equations for excited states and it is given by

$$U^{pol} = (\phi_0|PVQG^{(+)}_{QQ}QVP|\phi_0)\,. \tag{42}$$

Above, $P = |\phi_0)(\phi_0|$ is the projector on the elastic channel, $Q = 1-P = \sum_{\alpha\neq 0}|\phi_\alpha)(\phi_\alpha|$, and the propagator $G^{(+)}_{QQ}$ is defined as

$$G^{(+)}_{QQ} = \frac{1}{E - QH_0Q + i\epsilon}\,. \tag{43}$$

The wave function is then obtained by solving

$$(E - H_0 - U^{pol})|\psi_0\rangle = 0\,, \tag{44}$$

which, in the position representation is written

$$\left[E - T - U^{opt}(\mathbf{r})\right]\,\psi(\mathbf{r}) - \int U^{pol}(\mathbf{r},\mathbf{r}')\;\psi(\mathbf{r}')d^3\mathbf{r}' = 0\,, \tag{45}$$

where $U^{pol}(\mathbf{r},\mathbf{r}')$ is the nonlocal potential

$$U^{pol}(\mathbf{r},\mathbf{r}') = \sum_\alpha V_{0\alpha}(\mathbf{r})\,G^{(+)}(E_\alpha;\mathbf{r},\mathbf{r}')\,V_{\alpha 0}(\mathbf{r}')\,. \tag{46}$$

In principle, evaluating the polarization potential is nearly as hard as solving the coupled channel equations. However, for practical purposes it is replaced by trivially equivalent local potentials, which are calculated with approximations[20, 21].

4.2 Fusion and breakup cross sections

With the introduction of the polarization potential, any flux going away from the elastic channel is treated as absorption. The sum in Eq. (41) is then reduced to a single term, the one with $\alpha = 0$. The imaginary part of the potential is (henceforth we drop the superfluous index α, since only the elastic channel appears),

$$W = W^{opt} + W^{pol}\,, \tag{47}$$

the absorption cross section can be split as

$$\sigma_a = \sigma_F + \sigma_{bu}\,. \tag{48}$$

Above,

$$\sigma_F = \frac{k}{E}\int d^3\mathbf{r}\;W^{opt}(r)\;|\psi(\mathbf{r})|^2 \tag{49}$$

is identified with absorption through complete fusion and

$$\sigma_{bu} = \frac{k}{E}\int d^3\mathbf{r}\;W^{pol}(r)\;|\psi(\mathbf{r})|^2 \tag{50}$$

corresponds to the loss of flux through the breakup channel. It includes the breakup cross section and also a cross section for absorption in the breakup channels, probably incomplete fusion. However, since for weakly bound nuclei the range of W^{pol} is much larger than that of W^{opt}, we neglect this contribution and use the notaton σ_{bu} in Eq. (50).

It is useful to consider the expansion in partial waves of the wavefunction,

$$\psi = \sum_{l,m} \frac{u_l(k,r)}{r} Y_{lm}(\theta,\varphi)\,, \tag{51}$$

where $k = \sqrt{2\mu E/\hbar^2}$ and the $u_l(k,r)$ are solutions of the radial equation,

$$-\frac{\hbar^2}{2\mu}\left[\frac{d^2}{dr^2} - \frac{l(l+1)}{r^2}\right] u_l(k,r) + U^{opt}(r)\, u_l(k,r) = E\, u_l(k,r)\,, \tag{52}$$

normalized such that

$$u_l(k, r\to\infty) = \frac{i}{2}\left[H_l^{(-)}(kr) - S_l\, H_l^{(+)}(kr)\right]\,. \tag{53}$$

Using the partial wave expansion in Eq.(49), the fusion cross section may be rewritten as

$$\sigma_F = \frac{\pi}{k^2}\sum_l (2l+1) T_l^F\,, \tag{54}$$

where the transmission coefficient is given by

$$T_l^F = 1 - |S_l|^2 = \frac{4k}{E}\int_0^\infty dr\ W^{opt}(r) \| u_l(k,r)|^2\ .r \tag{55}$$

Proceeding similarly with Eq. (50), we get

$$\sigma_{bu} = \frac{\pi}{k^2}\sum_l (2l+1) T_l^{bu}\,, \tag{56}$$

with

$$T_l^{bu} = \frac{4k}{E}\int_0^\infty dr\ W^{pol}(r) |u_l(k,r)|^2\,. \tag{57}$$

4.3 Approximations

In what follows, we study different approximations to the coefficients T_l^F and T_l^{bu}. In order to fix ideas, we consider a ^{11}Li beam incident on a ^{12}C target, using an optical potential $U^{opt} = V^{opt} - i\, W^{opt}$ parameterized in the standard way:

$$V^{opt}(r) = V^N(r) + V^C(r)\,, \tag{58}$$

with the nuclear part given by

$$V^{opt}(r) = \frac{V_0^{opt}}{1 + \exp\left[(r - R_r)\ /a_r\right]}\,, \tag{59}$$

and the Coulomb one by

$$\begin{aligned} V^{Cou}(r) &= Z_p Z_t e^2/r; && \text{for } r > R_C \\ &= \left(Z_p Z_t e^2/2R_C\right)\ \left[3 - \left(\frac{r}{R_C}\right)\right]^2; && \text{for } r \leq R_C\,. \end{aligned} \tag{60}$$

Above, Z_p, A_p (Z_t, A_t) are the atomic and mass numbers of projectile (target), e the electron charge, R_C the radius of the nuclear charge distribution, and

$$R_{r,i} = r_{r,i}^0\ \left(A_p^{1/3} + A_t^{1/3}\right)\ .$$

The imaginary part is similarly parameterized as

$$W^{opt}(r) = \frac{W_0^{opt}}{1 + \exp\left[(r - R_i)\ /a_i\right]}\,. \tag{61}$$

We take the following parameter values:

$$V_0^{opt} = -60\ \text{MeV}; \quad r_r^0 = 1.25\ \text{fm}; \quad a_r^0 = 0.60\ \text{fm}\,; \tag{62}$$

$$W_0^{opt} = 60\ \text{MeV}; \quad r_i^0 = 1.00\ \text{fm}; \quad a_i^0 = 0.60\ \text{fm}\,. \tag{63}$$

Note that, since W^{opt} corresponds exclusively to short range fusion absorption, r_i^0 is appreciably smaller than r_r^0.

In order to review the standard approximations in the optical potential calculations, we initially disconsider the breakup channels. In the absence of breakup, the imaginary part of the nuclear potential has a short range, and therefore fusion may be approximately described through an infinitely absorbing imaginary potential with a well defined radius R_F. In this case T_l^F may be estimated by T_l, the transmission coefficient through the effective potential

$$V_l(r) = V^{opt}(r) + \frac{\hbar^2}{2\mu}\frac{l(l+1)}{r^2}\,. \tag{64}$$

If one approximates the region around the maximum of V_l by a parabola, then one obtains the Hill-Wheeler expression for T_l^F [2]

$$T_l^F \approx T_l \approx T_l^{HW} = \left\{1 + \exp\left[2\pi\left(\frac{B_l - E}{\hbar\omega_l}\right)\right]\right\}^{-1}\,, \tag{65}$$

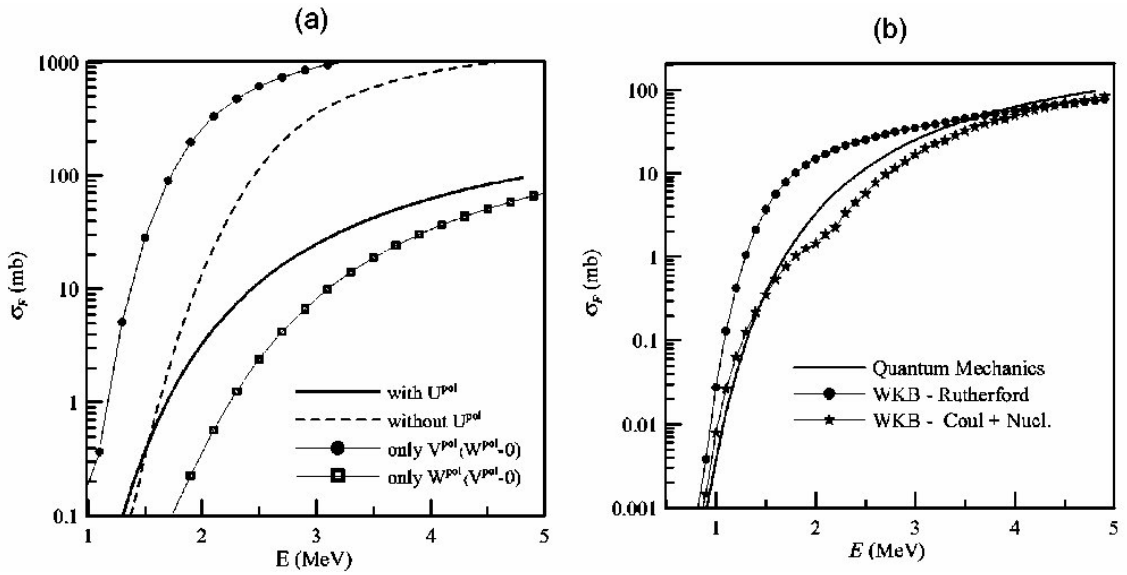

Figure 6 (a) Fusion cross section with different contributions of the polarization potential. See text for details. (b) Fusion cross sections obtained with different approximations employed in previous publications. The solid line indicates exact quantum mechanical calculations and the remaining ones are obtained with survival probability approximation (Eq. (75)). The solid circles were obtained with Rutherford trajectories whilethe starts were obtained with classical trajectories taking into account both the Coulomb and the nuclear potentials.

where R_B is the position of this maximum, B_l its value, and ω_l the curvature of V_l at $r = R_B$,

$$\hbar\omega_l = \left(- \frac{\hbar^2}{\mu} \left[\frac{d^2 V_l(r)}{dr^2} \right]_{R_B} \right)^{1/2} . \tag{66}$$

In Fig. 5(b), we show an example of a cross section calculated within the Hill-Wheeler approximation (dashed line) compared with the exact quantum mechanical calculation (full circles). One notices that the approximation is excellent at energies above the Coulomb barrier, $E > V_B \equiv B_{l=0}$, but worsens rapidly for $E << V_B$.

The problem at low energies may be improved using the WKB approximation. The transmission factor is then given by

$$T_l \approx \exp(-2\Phi) \tag{67}$$

where

$$\Phi = \mathrm{Im} \left\{ \int_{r_{in}}^{r_{out}} k(r) dr \right\} . \tag{68}$$

Above,

$$k(r) = \frac{1}{\hbar}\,\sqrt{2\mu\ [E - V_l(r)]} \tag{69}$$

and r_{in} e r_{out} are the inner and outer classical turning points for the potential V_l, determined through the condition $V_l(r_{in(out)}) = E$. However, this approximation is not good at energies $E \approx B_l$; for $E = B_l$ it yields $T_l = 1$ instead of the correct value $T_l = 1/2$, and even worse, it does not predict reflections above the barrier. Improvement is obtained by substituting the approximation of Eq. (67) by Kemble's expression [29] below the barrier while keeping Hill-Wheeler's approximation above it,

$$T_l = (1 + e^{2\Phi})^{-1}\ (E < B_l); \qquad T_l = T_l^{HW}\ (E \geq B_l). \tag{70}$$

This appproximation has been employed in Ref. [12]; it is equivalent to employing the Hill-Wheeler formula for all energies, albeit with the modification

$$\frac{\pi}{\hbar\omega_l}(B_l - E) \longrightarrow \Phi; \quad \text{for } E > B_l\,.$$

The cross section obtained within this approximation is depicted in Fig. 5(b) (solid line). We see that it reproduces the full quantum calculations for all collision energies.

Let us now consider the inclusion of the breakup channels. As we have seen, this may be done through the introduction of an appropriate polarization potential. Such potentials were studied in Refs. [17, 18], for pure nuclear coupling, and in [19, 21] for the electromagnetic coupling. In [17, 18] only the imaginary part of the polarization potential was calculated. Since the real part of the polarization potential reduces the height of the potential barrier, this effect was simulated by a shift in the collision energy in the calculation of T_l. Namely,

$$T_l(E) \rightarrow T_l(E + \Delta E); \quad \Delta E = -\,V^{pol}(R_B)\,.$$

As we will see, the real part of the polarization potential plays a very important role at energies below the Coulomb barrier. In the case of ^{11}Li + ^{12}C, the breakup process is dominated by the nuclear coupling. Therefore we write

$$W^{pol}(r) = \frac{W_0^{pol}(l, E_{CM})}{1 + \exp\left[(r - R_{pol})/\alpha\right]}\,, \tag{71}$$

where R_{pol} may be approximated by the optical potential radius, and the diffuseness α is given in terms of the breakup threshold energy B_{bu} as

$$\alpha = \left(\frac{2\mu_{bu}B_{bu}}{\hbar^2}\right)^{1/2}\,. \tag{72}$$

Above, μ_{bu} is the reduced mass of the fragments produced in the breakup process. In the case of ^{11}Li, $B_{bu} = 0.2$ MeV and thus $\alpha = 6.6$ fm.

The strength of the polarization potential varies with l and E_{CM}, and, for the partial waves relevant to the fusion process, is of the order of 1 MeV in the region around $r \approx R_{pol}$. Since we are not concerned with its derivation, but with the approximations employed in the determination of the cross section, let us adopt the constant value

$$W_0^{pol}(l,E) \equiv W_0^{pol} = 2.0\,\mathrm{MeV}\,. \tag{73}$$

Since the real part of the polarization plays a very important role at energies below the Coulomb barrier, we shall include it here. In the calculations of Ref. [21] the real and imaginary parts of the polarization potential have qualitatively the same strengths. For simplicity we then take them to be equal, *i.e.*

$$V_0^{pol}(l,E) \equiv V_0^{pol} = -2.0\,\mathrm{MeV}\,. \tag{74}$$

The effect of the real and imaginary parts of the polarization potential are shown in Fig. 6(a). As it could be expected, the real part leads to a substantial increase in the fusion cross section, most evident at energies below the Coulomb barrier. On the other hand, the imaginary part reduces the cross section both above and below the barrier. When both the real and imaginary parts are included, there is a competition between the effects of the real and imaginary parts. With the polarization strength values considered above, suppression dominates above the barrier and enhancement below it. This situation was also encountered in the coupled channels calculations of Refs. [23] and [24].

The presence of a long-ranged absorption requires the introduction of modifications in the approximations to T_l^F. Now the flux that reaches the strong absorption region is attenuated not only because of the reflection at the barrier, but also because of its absorption into the breakup channel. In Ref. [16] it was proposed the approximation

$$T_l^F \approx T_l(E+\Delta E)\cdot P_l^{surv}\,, \tag{75}$$

where $T_l(E+\Delta E)$ is the WKB transmission factor (Eq. (67)) evaluated at the energy $E+\Delta E$ and P_l^{surv} is the breakup survival probability. Within the WKB approximation we may take

$$P_l^{surv} = \exp\left[-\frac{2}{\hbar}\int \frac{W^{pol}(r)}{\mathrm{v}_l(r)}dr\right]\,, \tag{76}$$

where $\mathrm{v}_l(r)$ is the local radial velocity along a classical trajectory with angular momentum $\hbar l$. A more formal justification for Eq (75), based on a WKB calculation with three turning points was presented in Ref. [18]. This approximation is consistent with the results of Fig. .6(a) The enhancement due to V^{pol} is incuded in T_l while the suppression arising from W^{pol} is contained in P_l^{surv}.

In order to estimate P_l^{surv} one needs to define the classical trajectories to be employed in the calculation. In Ref. [16] pure Rutherford trajectories were considered, neglecting the nuclear potential diffractive effects. These trajectories present a single

turning point. The corresponding fusion cross section is shown in Fig. 6(b) as a thin line with solid circles. This figure also depicts the full quantum mechanical results (thick sodlid line). We see that although the approximation obtained with the Rutherford trajectory is reasonable at high energies, it breaks down at energies close and below the Coulomb barrier ($V_B = 2.67$ MeV). The inclusion of the nuclear potential in the trajectory calculations improves considerably the results (thin line with stars). In this case we may have, depending on the partial wave and collision energy, one or three turning points. The treatment with three turning points is not accurate in the region around the Coulomb barrier, and that is the reason why there are large deviations in the approximated fusion cross section. Later we will show how one may improve this approximation, but let us first briefly consider the breakup cross section.

In Ref. [16] the breakup was calculated by considering that

$$T_l^{bu} = 1 - P_l^{surv} \,. \tag{77}$$

This approximation is based on the notion that T_l^{bu} corresponds to the probability of non-survival to the breakup process. The results depend strongly on the classical trajectory considered. In Fig. 7(a) we compare the exact quantum mechanical breakup cross section to the ones obtained using Eq. (77) with different trajectories. The results are far from satisfactory. In particular, when the nuclear potential is included in the trajectory calculations the low energy breakup cross section has a completely wrong behavior. The reason for this discrepancy has been discussed by Ref. [18] and will be considered in further detail later in this section.

Let us now develop an improved WKB approximations for T_l^F and T_l^{bu}. In order to explain them, it will be useful to rewrite the T_l^F coefficients in a different way. In the WKB approximation, the radial wave funcions with incoming $(-)$ and outgoing $(+)$ boundary conditions are given by

$$u_l^{(\pm)}(r) = \frac{A}{\sqrt{k(r)}} \exp\left[\pm i \int dr \; k(r)\right] \,, \tag{78}$$

where

$$k(r) = \frac{1}{\hbar}\sqrt{2\mu\left[E - U^{opt}(r) - \frac{\hbar^2}{2\mu r^2} l(l+1) - U^{pol}(r)\right]} \,. \tag{79}$$

The value of T_l^F is given by the ratio between the probability density current that reaches the strong absorption region, $j^{(-)}(r = R_F)$, to the incident one $j^{(-)}(r = \infty)$, where the radial currents are

$$j^{(\pm)}(r) = \frac{\hbar}{2\mu i}\left[\left(u_l^{(\pm)}(r)\right)^* \left(\frac{du_l^{(\pm)}(r)}{dr}\right) - u_l^{(\pm)}(r)\left(\frac{du_l^{(\pm)}(r)}{dr}\right)^*\right] \,. \tag{80}$$

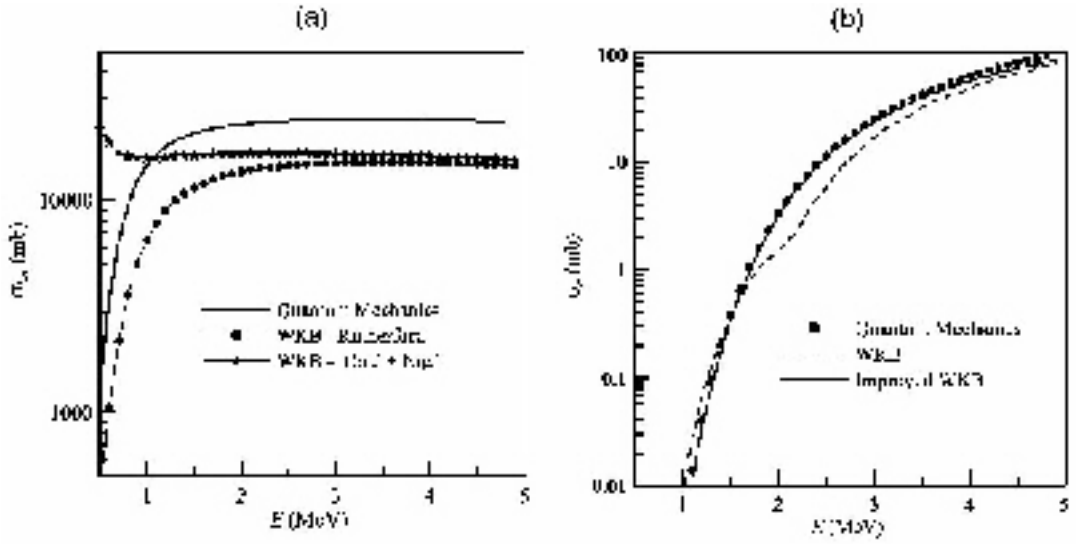

Figure 7 (a) Exact breakup cross section (solid line) and and cross sections approximated by Eq. (77). The solid circles were obtained with pure Rutherford trajectories while the stars takes into account nuclear potential effects on the trajectory. (b) Exact complete fusion cross section (solid circles) compared to the old approximation, depicted also in Fig. 6(b) (stars), and with the improved WKB approximation (solid line). See text for more details.

From Eqs.(78) to (80), we obtain

$$T_l^F = \frac{j^{(-)}(r = R_F)}{j^{(-)}(r = \infty)} \approx \exp\left[-2\bar{\Phi}\right] , \tag{81}$$

where

$$\bar{\Phi} = \mathrm{Im}\left\{\int_{R_F}^{\infty} dr\, k(r)\right\} . \tag{82}$$

If one does not include the polarization potential, the integrand in the equation above is real on the whole classically allowed region (note that $W^{opt}(r > R_F) = 0$). In this way, only the classically forbidden region contributes to attenuate the current that reaches the fusion region ($r < R_F$), *i.e.*

$$\bar{\Phi} \to \Phi = \int_{r_{in}}^{r_{out}} dr\, k(r) , \tag{83}$$

where r_{in} and r_{out} are the inner and outer turning points. In this case T_l^F reduces to the expression given in Eq. (67).

However, if there is long-ranged absorption as a result of the coupling to the breakup channels, the integrand in Eq. (82) becomes complex in all the integration region. The contributions to the integral that defines $\bar{\Phi}$ from the classically allowed

and forbidden regions may be calculated separately. In this case, T_l^F is written as the product of factors resulting from each of them. Disregarding the imaginary part of $U^{pol}(r)$ in the classically forbidden region, the corresponding factor reduces to the WKB tunneling probability T_l. On the other hand, in the classically allowed regions $k(r)$ can be calculated in an approximate way. Assuming that the imaginary part of $U^{pol}(r)$ is small in comparison to the remaining terms in the square root appearing in Eq. (79), we may take a series expansion to the lowest order,

$$k(r) \simeq k_0(r) + i \, \frac{W^{pol}(r)}{\hbar \, \mathrm{v}(r)} \, , \tag{84}$$

where

$$k_0(r) = \frac{1}{\hbar} \sqrt{2\mu \left[E - U^{opt}(r) - \frac{\hbar^2}{2\mu r^2} l(l+1) - V^{pol}(r) \right]} \tag{85}$$

and $\mathrm{v}(r)$ is the local velocity,

$$\mathrm{v}(r) = \frac{\hbar k_0(r)}{\mu} \, . \tag{86}$$

Since $k_0(r)$ does not attenuate the incident probability current, we obtain the same factor P_l^{surv} as before.

In our procedure we do not explicitly distinguish between classically allowed and forbidden regions, and calculate $\bar{\Phi}$ directly from Eq. (82), without any of the additional approximations mentioned in the previous paragraph. Fig. 7(b) shows the fusion cross section obtained within this approximation, compared with the exact results and with the old approximation. We see that the present approximation yields excellent results in all energy regions, including the one around the Coulomb barrier where the old approximation totally failed.

As noted in Ref. [18], the relationship between T_l^{bu} and P_l^{surv} that appears in Eq. (77) is not actually correct. The reason for this is that when we calculate the survival probability we consider only the incident branch of the trajectory, along which the system approaches the strong absorption region. However, the breakup process may take place both on the entrance or exit branches. Let us first consider the calculation of Ref. [16], which determines P_l^{surv} along a Rutherford trajectory. The survival probability associated with T_l^{bu} is the one calculated along the whole trajectory, *i.e.* along both branches A and B in Fig. 8(I-a), and not just along branch A, as it was done in the calculation of P_l^{surv}. Since the contribution from both branches to the integral that defines $\bar{\Phi}$ (Eq. (82)) are equal, the breakup probability amplitude may be written as

$$T_l^{bu} = 1 - \left(P_l^{surv} \right)^2 \, . \tag{87}$$

If we now take into account the effect of the nuclear potential on the classical trajectory, the situation changes very much. For low partial waves, where $E > B_l$,

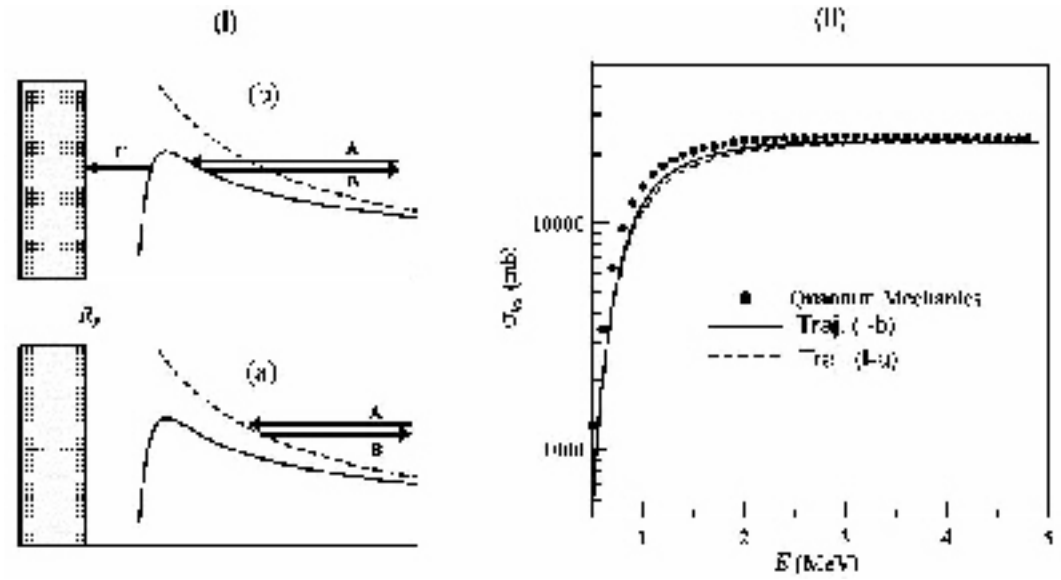

Figure 8 (I) Branches (A, incoming; B, outgoing) of the collision trajectory that contribute to the breakup process, (a) pure Rutherford, and (b) including nuclear potential effects. In this later case, the incoming branch has an additional segment (C). (II) Exact calculations of the breakup cross section (solid circles) compared to WKB calculations taking into account all branches of the classical trajectory (A, B, C of left figure(b) and Eq. (91)) (solid line) and taking only branches A and B in the Rutherford trajectory (left figure - a) and Eq. (87)) (dashed line).

the infinite absorption condition in the strong absorption region allows for only an ingoing branch. On the other side, for partial waves for which $E < B_l$ we may have two classical turning points, as illustrated in Fig.8(I-a). In that case all segments A, B, C do contribute to the breakup cross section. In this case the amplitude T_l^{bu} is given by

$$T_l^{bu} = \frac{\left[j_l^{(-)}(\infty) - j_l^{(-)}(r_{out})\right] \; + \; \left[j_l^{(-)}(r_{in}) - j_l^{(-)}(R_F)\right] \; + \; \left[j_l^{(+)}(r_{out}) - j_l^{(+)}(\infty)\right]}{j_l^{(-)}(\infty)} \, . \tag{88}$$

The first term in the numerator corresponds to the contribution to the breakup channel along incoming branch A in Fig. 8(I-b). The second term corresponds to the other incoming segment, C, while the third one is the contribution associated to the exit

branch B. The currents in this equation are given by

$$\begin{aligned} j_l^{(-)}(r_{out}) &= e^{-2\Phi_1}\; j_l^{(-)}(\infty) \\ j_l^{(-)}(r_{in}) &= T_l\; j_l^{(-)}(r_{out}) \\ j_l^{(-)}(R_F) &= e^{-2\Phi_2}\; j_l^{(-)}(r_{in}) \\ j_l^{(+)}(r_{out}) &= (1-T_l)\; j_l^{(-)}(r_{out}) \\ j_l^{(+)}(\infty) &= e^{-2\Phi_1}\; j_l^{(-)}(r_{out})\,, \end{aligned} \tag{89}$$

where Φ_1 e Φ_2 are given by

$$\Phi_1 = \mathrm{Im}\left\{\int_{r_{out}}^{\infty} dr\, k(r)\right\}\;; \quad \Phi_2 = \mathrm{Im}\left\{\int_{r_{in}}^{r_{out}} dr\, k(r)\right\}. \tag{90}$$

Substituting the density currents in Eq. (88), we obtain

$$T_l^{bu} = \left[1-e^{-2\Phi_1}\right] + e^{-2\Phi_1}\left[T_l\,\left(1-e^{-2\Phi_2}\right) + (1-T_l)\,\left(1-e^{-2\Phi_1}\right)\right]. \tag{91}$$

The breakup cross section calculated using Eqs. (87) (dashed line) and (91) (full line) are shown in Fig. 8(II), where they are compared to exact results (solid circles). We notice that the two approximations lead to similar results, and both are reasonably close to the exact values. Comparing the two curves we reach two important conclusions. One is that the inaccuracy in the results in Fig. 7(a) is due to the omission of the exit branch in the trajectories. The other is that in the present case nuclear effects on the trajectory are not very relevant. This is because the most important contributions to the breakup cross section arise from the high-l partial waves. While for the energy range considered the fusion cross section converges for $l = 10$, the breakup one requires the inclusion of partial waves as high as $l \approx 80$. In this way, for most partial waves relevant for the breakup calculation the external turning point is placed outside the nuclear potential range. The situation changes somewhat when a more realistic potential is considered. In that case, its intensity decreases at high l values, and the breakup cross section becomes more sensitive to low partial waves.

1. H. Bethe, Phys. Rev. **55** (1939) 434.
2. D.L. Hill and J.A. Wheeler, Phys. Rev. **89** (1953) 1102.
3. C.Y. Wong, Phys. Rev. Lett. **31** (1973) 766.
4. U. Mosel, Comm. Nucl. Part. Phys. **9** (1981) 213.
5. S.M. Lee, T. Matsuse and A. Arima, Phys. Rev. Lett. **45** (1980) 165.
6. R.G. Stokstad, Y. Elisen, S,. Kalanis, D. Pelte, U. Smilanski and I. Tserruya, Phys. Rev. Lett. **41** (1978) 465.
7. A.B. Balantekin and M. Takigawa, Rev. Mod. Phys. **70** (1998) 77.
8. A.B. Balantekin, S.E. Koonin and J.W. Negele, Phys. Rev. **C38** (1983) 1565.

9. N. Rowley, G.R. Satchler and P.H. Stelson, Phys. Lett. **B254** (1991) 25.
10. S. Björnholm and W.J. Swiatecki, Nucl. Phys. **A391** (1982) 471.
11. J.R. Leigh et al. Phys. Rev. **C52** (1995) 3151.
12. L.F. Canto, R. Donangelo, Lia M. Matos, M.S. Hussein and P. Lotti, Phys. Rev. C**58** (1998) 1107.
13. M. Trotta *et al.* Phys. Rev. Lett. **84** (2000) 2342.
14. J.J. Kolata *et al.* Phys. Rev. Lett. **81** (1998) 4580.
15. K.E. Rehm *et al.* Phys. Rev. Lett. **81** (1998) 3341.
16. M.S. Hussein, M.P. Pato, L.F. Canto and R. Donangelo, Phys. Rev. **C46** (1992) 377.
17. M.S. Hussein, M.P. Pato, L.F. Canto and R. Donangelo, Phys. Rev. **C47** (1993) 2398.
18. N. Takigawa, M. Kuratani and H. Sagawa, Phys. Rev. **C47** (1993) R2470.
19. L.F. Canto, R. Donangelo, P. Lotti and M.S. Hussein, Phys. Rev. **C52** (1995) R2848.
20. L.F. Canto and R. Donangelo, M.S. Hussein and M.P. Pato, Nucl. Phys. **A542** (1992) 131.
21. M.V. Andrés, J. Gómes-Camacho and N.A. Nagarajan, Nucl. Phys. **A579** (1994) 573.
22. C.H. Dasso and A. Vitturi, Phys. Rev. **C50** (1994) R12.
23. A.M.S. Breitschaft, V.C. Barbosa, L.F. Canto, M.S. Hussein, E.J. Moniz, J. Christley and I.J. Thomson, Ann. of Phys. **243** (1995) 420.
24. K. Hagino, A. Vitturi, C.H. Dasso and S. Lenzi, Phys. Rev. **C61** (2000) 037602.
25. J. Takahashi et al., Phys. Rev. Letters **78** (1997) 30.
26. G.R. Satchler, 'Direct Nuclear Reactions', Oxford University Press, 1983.
27. G.R. Satchler, Phys. Rev. **C32** (1985) 2203.
28. H. Feshbach, Ann. Phys. **19** (1962) 287
29. E.C. Kemble, Phys. Rev. **48** (1925) 549.

Fusion of Very Heavy Nuclei

5 Introduction

Contrary to the sub-barrier fusion enhancement found in light + heavy systems, the fusion of very heavy systems of the type employed in the production of superheavy elements (SHE), shows hindrance when compared to the simple one-dimensional barrier penetration model. The incident energy has be much higher than the fusion barrier which accounts for fusion of lighter systems, in order for heavy element production to proceed. One needs an *extra push*, as proposed by Björnholm and Swiatecki [1]. This extra energy needed for fusion to occur comes about from the fact that the fission barrier for massive systems is located inside the potential barrier in the entrance channel. Björnholm and Swiatecki (BS) introduced the term *extra-push*; the

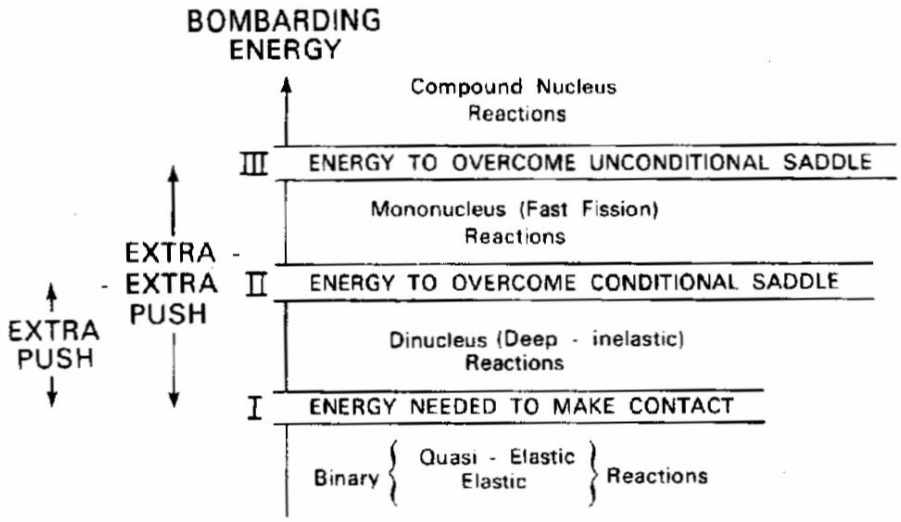

Figure 9 Schematic illustration of the relation between three critical energies, four types of nuclear reactions, and two kinds of extra push. This figure is appropriate when the three milestone configurations discussed in the text exist and are distinct. In some situations the critical energies I, II, III may merge (pairwise or all together) squeezing out the regimes corresponding to dinucleus and/or mononucleus reactions. In other situations one or both of the upper boundaries (II and III) may dissolve, making the adjoining regions merge into continuously graduated reaction types.

energy needed to overcome the saddle point in the potential energy surface under the constraint of mass asymmetry, and the *extra-extra-push* which is the energy needed to carry the system beyond (inside) the fission saddle point. We shall discuss the BS model. The hinderance of the fusion cross section for very heavy systems can be accounted for using a formula similar to the Glas-Mosel model. A very nice account of such a calculation has been recently given by Smolanczuk [2]. The discussion in these sections is important for the genral account of *Super Heavy Element*s (SHE).

6 The extra push and the extra-extra push

The schematic model of Ref. [3] illustrated the expectation that there should often be three configuration of special importance – three milestones – in the dynamical evaluation of a nucleus-nucleus collision. These three milestone configurations, which define three associated threshold energies, are as follows:

I - *The contact configuration*, where the two nuclei come into contact and the growth of a neck between them becomes energetically favourable. This type I configuration is usually close to the top of the interaction barrier in a one-dimensional plot of the potential energy of two approaching nuclei, whose den-

sities are assumed to be frozen. (It would coincide *exactly* with the top of the barrier if the nuclear surfaces were sharp and the range of nuclear forces were neglected). However, for systems with sufficient electric charge and/or angular momentum, the maximum in the (effective) interaction may disappear, but the contact configuration is expected to retain its milestone significance associated with the rather sudden unfreezing of the neck degree of freedom around contact.

II - *The configuration of conditional equilibrium* (a saddle -point pass) in a multidimensional plot of the potential energy at frozen mass asymmetry. (The equilibrium is *conditional* because its energy is stationary only on condition that the asymmetry be held fixed). The physical significance of this type II milestone is proportional to the degree of inhibition of the mass-asymmetry degree of freedom, which in turn is related to the severity of the constriction (the smallness of the neck) in the conditional equilibrium shape. When the constriction is not severe, in particular when the shape is convex *everywhere, the type II configuration loses its physical significance as a milestone* configuration.

III - *The configuration of unconditional equilibrium* (the fission saddle-point shape). The associated fission barrier ensure the existence of a compound nucleus and guards it against disintegration. For a system with sufficient electric charge and/or angular momentum, the fission barrier disappears and a compound nucleus ceases to exist.

The type II and type III configurations are identical for mass-symmetric systems. They become substantially different only for sufficiently asymmetric systems.

In cases when all three milestone configurations exist, are distinct and physically significant, the three associated threshold energies suggest a division of nucleus-nucleus reactions into four more or less distinct categories (see Fig. 9):

(a) Reactions whose dynamical trajectories in configuration space do not overcome the type I threshold (i.e. trajectories that do not bring the nuclei into contact) lead to binary reactions (elastic and quasi-elastic scattering).

(b) Trajectories that overcome threshold I but not thresholds II and III correspond to dinucleus (deep-inelastic) reactions.

(c) Trajectories that overcome thresholds I and II but not III correspond to mononucleus (fast-fission) reactions.

(d) Trajectories that overcome thresholds I, II and III [and are trapped inside barrier III] correspond to compound-nucleus reactions.

We may note that in the idealization where the nuclear surfaces are assumed to be sharp and the range of nuclear forces is disregarded, there would be a clear-cut distinction between deep-inelastic and elastic reactions (looking apart, that is,

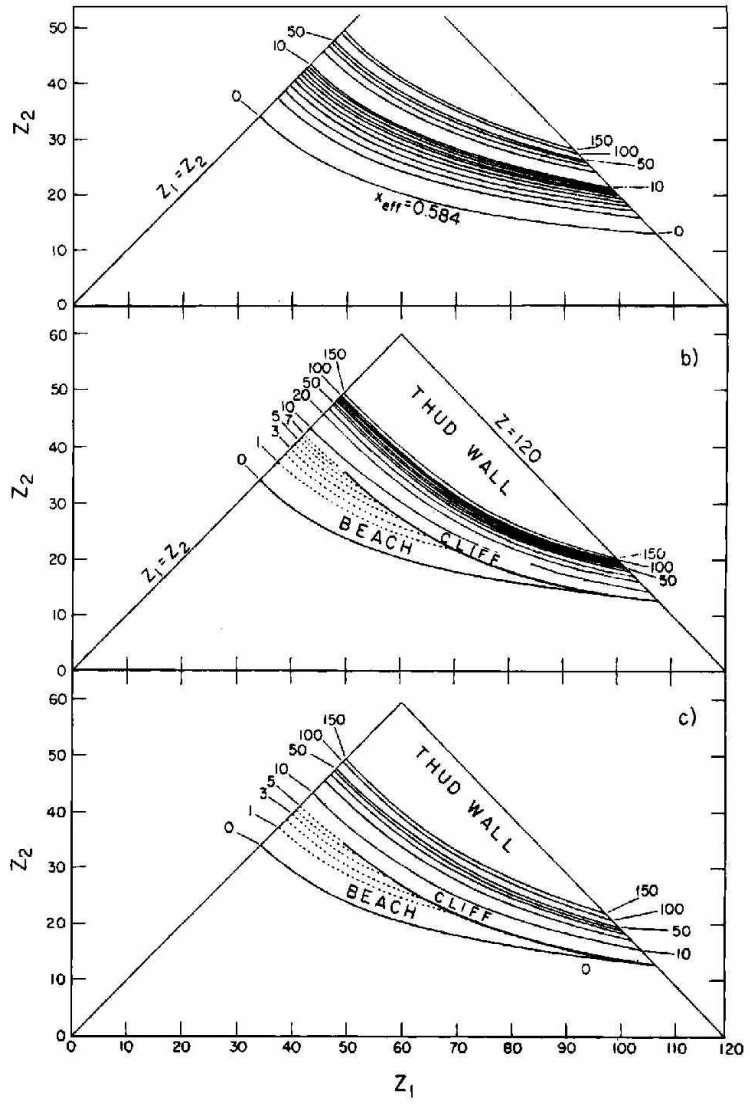

Figure 10 (a) Contour lines of the estimated extra push (in MeV) over the interaction barrier, needed to overcome the conditional saddle (i.e. the saddle at frozen asymmetry). For an asymmetric system and an injection energy beyond about the 10 MeV contour the conditional saddle begins to lose its physical significance because of the unfreezing of the asymmetry. The figure refers to the schematic model and must not be used for actual estimates. (b) Contour lines (in MeV) of the estimated extra-extra push over the interaction barrier needed to make a compound nucleus (or, at least, to form a spherical composite nucleus) out of two nuclei with atomic numbers Z_1 and Z_2. (Schematic model, not to be compared with experiment). (c) Contour lines of equal extra-extra push $E_{\chi\chi}$, using an analytic scaling formula fitted to the schematic model.

from inelasticities induced by electromagnetic interactions). This is illustrated in the model of Ref. [3] where, in their Fig. 6, trajectories that have resulted in contact are *discontinuously* different from those that have not. [The latter correspond to motion back and forth along the ρ-axis in Fig. 6 of Ref. [3]]. This leaves a blank space between the last elastic trajectory and the first deep-inelastic trajectory. With the diffuseness of the nuclear surfaces taken into account, this blank space would be filled out with trajectories that vary from binary (elastic) to dinucleus (deep-inelastic) reactions in a way that washes out the original discontinuity.

The degree of washing out is, however, proportional to the diffuseness of the surfaces, and it should be possible to maintain an approximate but useful distinction between elastic and deep-inelastic reactions to the extent that the leptodermous (thin-skin) approach to nuclear processes is approximately valid.

The qualitative consequences of the existence of the three milestone configurations were illustrated in the model of Ref. [3]. The physical ingredients of that model were:

(a) Conservative driving forces derived from a leptodermous (liquid-drop) potential energy:

(b) Dissipative forces derived from the chaotic-regime, one-body dissipation function in the form of the wall or wall-and-window formula;

(c) A schematic (reduced-mass) inertial force in the approach degree of freedom.

The model was further simplified by assuming the nuclear shapes to be parame trized as two spheres connected by a portion of a cone and by relaying heavily on the small-neck approximation and central collisions.

One consequence of the above model, which is obvious from qualitative considerations and had already been studied for symmetric systems in Ref. [4], is that for relatively light reacting nuclei the overcoming of the threshold I is sufficient to over-come barrier II, but that for heavier systems, or for systems with sufficient angular momentum, an "extra push" [an extra radial injection velocity over the threshold condition] is necessary. The upper part of Fig. 10 [taken from Ref. [5]] illustrates the dependence of the extra push (in MeV and for head-on collisions) on the atomic numbers Z_1, Z_2 of the reacting nuclei. In the schematic model used to construct the figure there emerges an approximate small-neck scaling parameter, the "effective fissility parameter" x_{eff}, proportional to the effective fissility $(Z^2/A)_{eff}$, and given by

$$\chi_{eff} = \left(Z^2/A\right)_{eff} / \left(Z^2/A\right)_{crit} \ , \tag{92}$$

where

$$\left(Z^2/A\right)_{eff} \equiv \frac{4Z_1Z_2}{A_1^{1/3}A_2^{1/3}\left(A_1^{1/3}+A_2^{1/3}\right)} \ , \tag{93}$$

$$\left(Z^2/A\right)_{eff} \equiv 2\left(4\pi r_0^2\gamma\right) / \left(\frac{3}{5}\frac{e^2}{r_0}\right) = \frac{40\pi r_0^3}{3e^2} \ , \tag{94}$$

$$\gamma = \gamma_0\left(1 - \kappa_s I^2\right) \ . \tag{95}$$

In the above equations, γ_0 is the surface-energy coefficient of standard nuclear matter, $I = (N-Z)/A$ is the relative neutron excess, e is the unit of charge, and κ_s is the surface symmetry energy coefficient. Using Ref. [6] we have

$$4\pi r_0^2\gamma_0 = 17.9439\, MeV \ , \qquad \frac{3}{5}\frac{e^2}{r_0} = 0.7053\, MeV \ , \qquad \kappa_s = 1.7826 \ ,$$

where r_0 is the nuclear radius parameter. It follows that an approximate expression for $\left(Z^2/A\right)_{crit}$ is

$$\left(Z^2/A\right)_{crit} = 50.883\left(1 - 1.78261^2\right) \ . \tag{96}$$

The parameter x_{eff}, proportional to Bass' parameter x [Ref. [7]], is a measure of the relative importance of electric and nuclear forces for necked-in configurations near contact. Its usefulness is illustrated by the fact that loci of equal extra push in the upper part of Fig. 10 are approximately loci of equal x_{eff} (approximately also loci of equal $\left(Z^2/A\right)_{eff}$).

The schematic model of Ref. [3] was also used to map out the "extra-extra push" over the interaction barrier, needed to overcome the unconditional barrier III (and form a compound nucleus). The result was presented in Fig. 6 of Ref. [5] and is reproduced here as the middle part of Fig. 10. For symmetric systems (along the diagonal $Z_1 = Z_2$) and in the region marked "beach" in Fig. 10, the extra-extra push is identical with the extra push, but for asymmetric systems, above the "cliff", the extra-extra push exceeds the extra push. One verifies readily that the loci of equal extra-extra push are no longer, even approximately, loci of equal x_{eff} or $\left(Z^2/A\right)_{eff}$. The reason is that, in the assault on the unconditional barrier III, the fusing system traverses regions of configuration space where its shape has no well-define neck or asymmetry and the small-neck scaling parameter x_{eff} is no longer relevant. In those regions the standard (total) fissility parameter x[or Z^2/A], where

$$\chi = \left(Z^2/A\right)\left(Z^2/A\right)_{crit} \ , \tag{97}$$

is the appropriate scaling parameter. Since, however, the trajectories in question traverse both the dinuclear and mononuclear regimes, neither x nor x_{eff} can be expected to be good scaling parameters. (In Fig. 2b, loci of constant x or Z^2/A would be approximately parallel straight lines corresponding to $Z_1 + Z_2 =$ constant).

The above circumstance appeared to put a serious limitation on a simple scaling-type exploitation of the results presented in Fig. 2b, until we realized that the use of a *mean scaling parameter* x_m, defined as a suitable mean between x and x_{eff}, reproduced approximately the loci of the calculated extra-extra push. A fair

representation is obtained by taking x_m to be simply the geometric mean, x_g, between x and x_{eff} (written x_e from now on), *viz.*:

$$\chi_m \approx \chi_g = \sqrt{\chi\chi_e} \propto \sqrt{\left(Z^2/A\right)\left(Z^2/A\right)_{eff}} \ . \tag{98}$$

A more flexible parametrization of the model calculations is obtained by making x_m deviate more rapidly from x with increasing asymmetry. Since the deviation of x_g from x is, in fact, itself a measure of asymmetry*, we have tried the following definition of x_m:

$$\chi_m = \chi\left[1 - \left(\frac{\chi-\chi_g}{\chi}\right) - k\left(\frac{\chi-\chi_g}{\chi}\right)^2\right] = \chi_g - k\chi\left(\frac{\chi-\chi_g}{\chi_g}\right)^2 \tag{99}$$

i.e.

$$\frac{\chi_m - \chi_g}{\chi} = -k\left(\frac{\chi-\chi_g}{\chi}\right)^2 \ ,$$

where k will be regarded as an adjustable parameter, controlling the deviation of χ_m from χ_g. Using an appropriate value of k we then constructed Fig. 2c according to the procedure explained in the following.

We start with the formula for the extra push (denoted by E_χ), which is obtained, according to Eq. (29) in Ref. [3], by writing the extra relative injection velocity - dr/dt, expressed in the natural velocity unit of the one-body dissipation dynamics, as a function ϕ, of the excess of the effective fissility parameter χ_e over threshold value χ_{th}:

$$\frac{-dr/dt}{2\gamma/\rho\bar{v}\bar{R}} = \phi\left(\chi_e - \chi_{th}\right) \approx a\left(\chi_e - \chi_{th}\right) + \text{ higher powers of } \left(\chi_e - \chi_{th}\right) \ , \tag{100}$$

where

$$a = \left.\frac{d\phi}{d\chi_e}\right|_{\chi_e=\chi_{th}} \ . \tag{101}$$

Here ρ is the nuclear matter density, $\bar{v}$ the mean nucleonic speed, $\bar{R}$ the reduce radius of the system $\left[\bar{R} = R_1R_2/\left(R_1+R_2\right)\right]$ and a is a constant (the derivative of ϕ evaluated at $\chi_e = \chi_{th}$). The threshold fissility parameter χ_{th} is a universal constant. The corresponding threshold value of $\left(Z^2/A\right)_{th}$ is given by

$$\left(Z^2/A\right)_{th} = \chi_{thZ^2}\left(Z^2/A\right)_{crit} \ . \tag{102}$$

Note that a fixed value of $\left(Z^2/A\right)_{th}$ only if the surface energy coefficient in Eq. 94 were a constant. Since, in fact, γ depends somewhat on the neutron excess, the threshold value of $\left(Z^2/A\right)_{th}$ is, in general, not quite the *same for different nuclear systems.*

*It may be verified from Eq. (1) in Ref.[8] that $\left(x - x_g\right)/x$ is equal to $1-\left(1-D\right)\left(1+3D\right)^{-\frac{1}{3}} \approx \frac{5}{2}D$, where D is a measure of asymmetry, given by the square of the difference between the gragment radii divided by their sum, i.e. $D = \left[\left(R_1-R_2\right)/\left(R_1+R_2\right)\right]^2$.

Denoting the reduce mass of the colliding system by M_r, we find for E_χ the expression

$$E_\chi = \frac{1}{2} M_r \left(\frac{dr}{dt}\right)^2 = E_{ch}\phi^2 \ , \tag{103}$$

where E_{ch} is a characteristic energy unit of the system, given by

$$\begin{aligned} E_{ch} &= \frac{2048}{91}\left(\frac{\pi}{3}\right)^{4/3} \frac{m\gamma^2 r_0^6}{\hbar^2} \frac{A_1^{\frac{1}{3}} A_2^{\frac{1}{3}} \left(A_1^{\frac{1}{3}} + A_2^{\frac{1}{3}}\right)^2}{A} \\ &= \frac{32}{2025}\left(\frac{3}{\pi}\right)^{2/3} \frac{me^4}{\hbar^2} \frac{A_1^{\frac{1}{3}} A_2^{\frac{1}{3}} \left(A_1^{\frac{1}{3}} + A_2^{\frac{1}{3}}\right)^2}{A} \left(\frac{Z^2}{A}\right)_{crit}^2 \\ &= 0.0007601 = \frac{A_1^{\frac{1}{3}} A_2^{\frac{1}{3}} \left(A_1^{\frac{1}{3}} + A_2^{\frac{1}{3}}\right)^2}{A} \left(\frac{Z^2}{A}\right)_{crit} \mathrm{MeV}^2 \ . \end{aligned} \tag{104}$$

[Compare Eqs. (30)-(33) in Ref. [3]]. Here m is the atomic mass unit ($mc^2 = 931.5\,\mathrm{MeV}$), and we have used the Fermi-gas expression for $\rho\bar{v}$:

$$\rho\bar{v} = \frac{27}{32\pi}\left(\frac{\pi}{3}\right)^{\frac{1}{3}} \frac{\hbar}{r_0^4} \ . \tag{105}$$

(This leads to the numerical estimate

$$\rho\bar{v} = 0.79744 \times 10^{-22}\, MeV \cdot \sec \cdot fm^{-4} \ , \tag{106}$$

if the value $r_0 = 1.2249\, fm$, implied by Ref. [6], is adopted for illustrative purposes).

Using for ϕ the linear approximation given by Eq. 100, we recover the formula for $E_\chi$quoted as Eq. (1) in Ref. [5].

The numerical calculations on which the upper part of Fig. 10 is based are approximately reproduced by a choice of χ_{th} equal to 0.584 and the following formula for ϕ:

$$\phi\left(\xi\right) = 5\xi + 27800\xi^7 \ . \tag{107}$$

(The linear term by itself is accurate to 10% up to $\xi \equiv \chi_e - \chi_{th} = 0.16$, after which it rapidly becomes inadequate). The numerical calculations of the extra-extra push $E_{\chi\chi}$ in the middle part of Fig. 10 were found to be reproduced approximately by changing the argument χ_e to χ_m, given by Eq. 99. Thus

$$E_{\chi\chi} = E_{ch}\phi^2\left(\chi_m - \chi_{th}\right) \ . \tag{108}$$

The result is shown in the lower part of Fig.10 for $k = 1$. The "cliff" in this figure is the locus where χ_m is a constant, i.e. $\chi_m = \chi_{c1} = 0.7$. This choice of χ_{c1} produces approximate agreement with Fig. 10 as regards the boundary where $E_{\chi\chi}$ exceeds E_χ.

The above formulae, which represent the results obtained with the aid of the schematic model of Ref. [3], can be made to reproduce approximately experimental data by using the linear approximation to ϕ together with empirically adjusted values of the parameters χ_{th} and a. This leads to the following semi-empirical formulae for the extra and the extra-extra push in head-on collisions:

$$\begin{aligned} E_\chi &= 0\,, && \text{for } \chi_e \leqq \chi_{th}\ , \\ E_\chi &\approx E_{ch}a^2\left(\chi_e-\chi_{th}\right)^2 = K\left(\zeta_e-\zeta_{th}\right)^2\ , && \text{for } \chi_e > \chi_{th}\ , \\ E_{\chi\chi} &= E_\chi\ , && \text{for } \chi_m \leqq c_{cl}\ , \\ E_\chi &= E_{ch}a^2\left(\chi_m-\chi_{th}\right)^2 = K\left(\zeta_m-\zeta_{th}\right)^2\ , && \text{for } \chi_m \leqq \chi_{cl}\ . \end{aligned} \tag{109}$$

In the above, ζ is a shorthand notation for Z^2/A and the constant K is given by

$$K = E_{ch}a^2/\zeta_{cr} = 0.0007601\frac{A_1^{\frac{1}{3}}A_2^{\frac{1}{3}}\left(A_1^{\frac{1}{3}}+A_2^{\frac{1}{3}}\right)^2}{A}a^2\,MeV\ . \tag{110}$$

For convenience, we collect together the definitions of the various symbols ζ and χ in the above equations. Thus the Z^2/A fissilities are given by

$$\begin{aligned} \zeta &= Z^2/A\ , \qquad \zeta_e = \left(Z^2/A\right)_{eff} \qquad \text{[see Eq. 93]}\ , \\ \zeta_g &= \sqrt{\zeta\zeta_e}\ , \qquad \zeta_m = \zeta_g - k\zeta\left(1-\frac{\zeta_g}{\zeta}\right)^2\ , \\ \zeta_{cr} &= \left(Z^2/A\right)_{crit} \quad \text{[see Eq. 94]}\ , \qquad \zeta_{th} = \chi_{th}\zeta_{cr} = b\left(1-k_sI^2\right)\ , \end{aligned} \tag{111}$$

where

$$\begin{aligned} b &= \frac{40\pi\gamma_0r_0^3}{3e^2}\chi_{th} = 50.883\chi_{th} = \begin{array}{c}\text{“threshold coefficient”}\\ \text{(a universal constant)}\end{array}\ , \\ \zeta_{cl} &= \chi_{cl}\zeta_{cr} = c\left(1-k_sI^2\right)\ , \end{aligned} \tag{112}$$

where

$$c = \frac{40\pi\gamma_0r_0^3}{3e^2}\chi_{cl} = 50.883\chi_{cl} = \begin{array}{c}\text{“cliff coefficient”}\\ \text{(a universal constant)}\end{array}\ . \tag{113}$$

The corresponding fissility parameters χ, χ_e, χ_g, χ_m, χ_{th} and χ_{cl} are obtained by dividing by $\left(Z^2/A\right)_{crit}$, as given by Eq. 94, *viz.*

$$\chi = \left(Z^2/A\right)\zeta_{cr}\,, \qquad \chi_e = \left(Z^2/A\right)_{eff}\zeta_{cr}\,, \tag{114}$$

$$\chi_g = \sqrt{\chi\chi_e}\,, \qquad \chi_m = \chi_g - k\chi\left(1-\frac{\chi_g}{\chi}\right)^2\ , \qquad \chi_{th},\,\chi_{cl} = \text{ universal constantes.} \tag{115}$$

There are altogether four dimensionless parameters in Eqs. (21)-(24), to be deduced from experiment or estimated from a dynamical model: a, χ_{th} (or b), χ_{cl} (or c), and k. Tables 1 gives some estimates of these parameters.

Note that the final formulae for the extra and extra-extra push may be written as follows:

$$\begin{aligned} E_\chi &= \frac{32}{2025}\left(\frac{3}{\pi}\right)^{2/3}\frac{e^4 m}{\hbar^2}\frac{A_1^{\frac{1}{3}}A_2^{\frac{1}{3}}(A_1^{\frac{1}{3}}+A_2^{\frac{1}{3}})^2}{A}a^2\left[\left(\frac{Z^2}{A}\right)_{eff}-b\left(1-k_sI^2\right)\right]^2 \\ &= 0.0007601\frac{A_1^{\frac{3}{2}}A_2^{\frac{1}{3}}(A_1^{\frac{1}{3}}+A_2^{\frac{1}{3}})^2}{A}a^2\left[\left(\frac{Z^2}{A}\right)_{eff}-b\left(1-k_sI^2\right)\right]^2 \text{MeV}\,, \\ & \quad 0.0007601\frac{A_1^{\frac{1}{3}}A_2^{\frac{1}{3}}(A_1^{\frac{1}{3}}+A_2^{\frac{1}{3}})^2}{A}a^2\left[\left(\frac{Z^2}{A}\right)_{m}-b\left(1-k_sI^2\right)\right]^2 \text{MeV}\,. \end{aligned} \quad (116)$$

The noteworthy feature of Eq. 117 is that, with the slope coefficient a and the threshold coefficient b determined empirically ($a = 12 \pm 2\, b = 35.62 \pm 1$), Eq. 117 is almost independent of any nuclear parameters. (The exception is the slight dependence on the surface symmetry energy coefficient k_s). In particular the surface energy coefficient γ_0 and the radius constant parameter r_0 do not appear explicitly, and no assumptions about their values need be made when applying Eq. 117. A similar remark applies to Eq. (42), but the relevant coefficients c and k [entering in $(Z^2/A)_m$] have not, so far, been determined empirically.

	Empirical	Schematic model [8]	Inproved model
Threshold fissility parameter χ_{th}	0.70 ± 0.02	0.584	$\approx 0.723^*$
Threshold coefficient b	35.62 ± 1		≈ 36.73
Slope coefficient a	12 ± 2	5	$\approx 18^*(or\ less^{**})$
Angular momentum fraction f	$\frac{3}{4} \pm 10\%$	$0.85 \pm 0.0.2^{***}$	
Cliff constant k		$k = 1$	
Cliff fissility parameter χ_{cl}	$(0.84 \lesssim \chi_{cl} \lesssim 0.86)^\dagger$	0.70	
Cliff coefficient c	$(42.7 \lesssim c \lesssim 43.8?)$		

* Deduced from J. Blocki *et al.*, private communication, 1981.

** H. Feldmeier, Ref. [9]: see text.

*** G. Fai, private communication, 1981.

† Further experimental evidence could be taken to suggest a somewhat lower value of χ_{cl}

Table 1 - Estimates of parameters.

The values $\chi_{th} = 0.723$, $a = 18$ in the last column of Table 1 were deduced from a model calculation by J. Blocki, in which the head-on collision of two equal sharp-surfaced nuclei was followed numerically using the chaotic regime dynamics. [The nuclear shapes were parametrized as spheres with a hyperbolic neck, Ref. [10]]. The total system was assumed to be on the valley of stability [i.e. $I = 0.4A/(200 + A)$] and the nuclear parameters were used according to which $(Z^2/A)_{crit} = 50.805\,(1 - 2.204I^2)$. Using this model, Blocki found that, starting with zero kinetic energy at contact, a system with mass number $A = 209$ would fuse, but for $A = 213$ it would reseparate having failed to overcome the saddle-point pass. Taking $A \approx 211\,(Z = 83.8353)$ as an estimate of the mass number corresponding to the threshold condition, one finds $\chi_{th} = \left[(83.83.53)^2\,211\right]/50.805\,(1 - 2.204I^2) = 0;723$, and $b = 50.805\chi_{th} = 36.73$.

In another set of numerical studies, Blocki found that a symmetric system with $A = 242\,(Z = 94.5005)$ needed about 40 MeV of extra push over the contact configuration to fuse. The effective fissility of this system is $\chi_e = 0.8122$. Using Eq. **??** it follows that

$$a \approx \sqrt{\frac{40\,Mev}{E_{ch}}}\,(\chi_e - \chi_{th})^{-1} \approx 18.0\,. \tag{117}$$

Feldmeier, Ref. [9], has pointed out that when the extra push is 40 MeV (and $\chi_e - \chi_{th}$ is of the order of 0.1) the nonlinearity in the dependence of $\sqrt{E_\chi}$ on $(\chi_e - \chi_{th})$ is appreciable and that if allowance were made for this, the value of a deduced from Blocki's calculation for $A = 242$ would be reduced.

Figs. 11((a) and (b)) illustrate Eqs. 109-110 for systems composed of two pieces with atomic numbers Z_1, Z_2 *each of which* is assumed to be on the valley of β-stability, as given by Green's formula, $N - Z = 0.4A^2/(200 + A)$. This makes the figures more nearly relevant to actual experimental situations than Fig. 10, where the *total system* was assumed to be on the valley of stability, and the implied projectiles have often quite unrealistic values of the neutron excess.

In constructing Figs. 11 we used the empirical values $\chi_{th} = 0.70$, $a = 12$ and the illustrative values $k = 1$, $\chi_{cl} = 0.84$. This value of χ_{cl} follows from rescaling the schematic model value $\chi_{cl} = 0.70$ by the factor 1.2, which is the ratio of the empirical to the schematic value of χ_{th} (i.e. $0.70 : 0.584 = 1.20$). The values $k = 1$, $\chi_{cl} = 0.84$ are also consistent with experimental indications discussed in the last paragraph of Sect. 13.3, which suggest $0.84 \lesssim \chi_{cl} \lesssim 0.86$. It cannot be stressed too emphatically, however, that the true values of k and χ_{cl} are simply not known at the present time. On the contrary, the schematic model is *known* to be quite inadequate for quantitative predictions and the rescaling by a factor 1.2 is open to question. Similarly the experimental indications concerning an upper limit on χ_{cl} are marginal at best and could be misleading. Hence the actual MeV values of the extra-extra push in Fig. 10, as well as the location of the cliff, are meant as qualitative illustrations only.

As in Refs. [11, 12, 13, 14]) we may generalize the expressions for E_χ to the case when an angular momentum L is present, by adding to the Coulomb potential

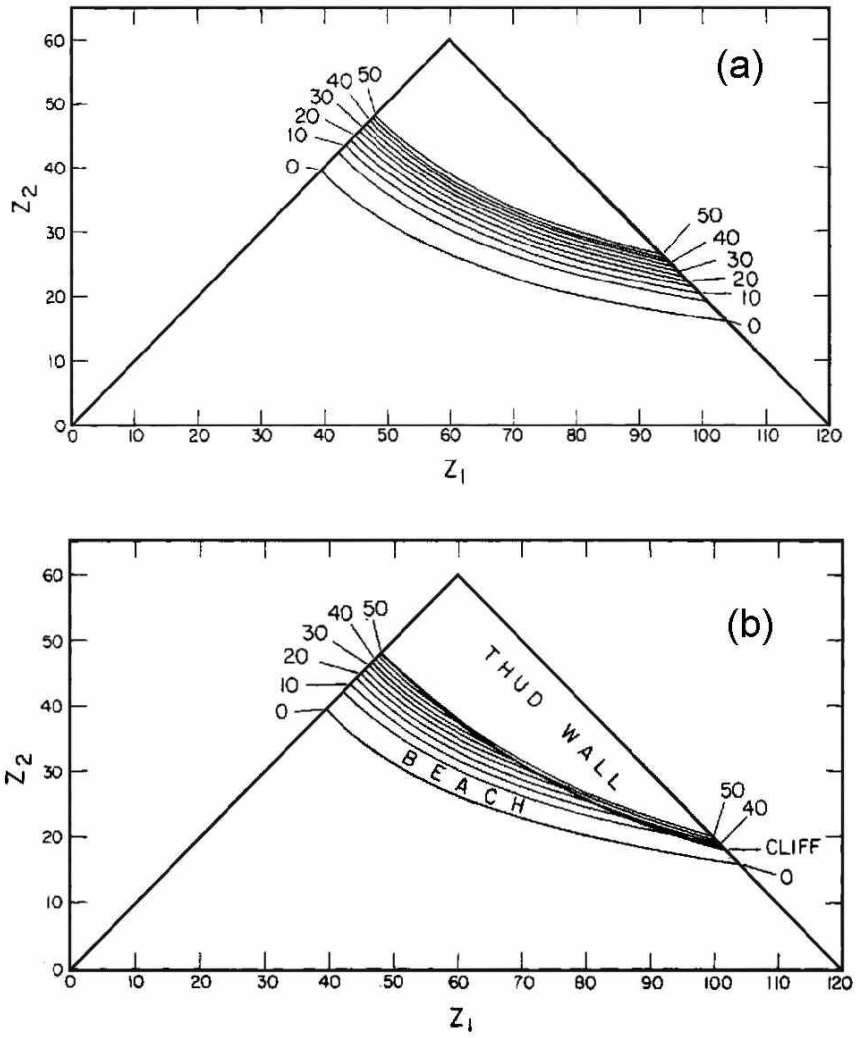

Figure 11 (a) Contour lines of the extra push according to Eq. 109, with parameters adjusted to reproduce the data of Ref. [4]. (b) Contour lines of equal extra-extra push. In the region below the cliff the contour lines are identical with the extra push in the upper part of this figure. Above the cliff, Eq. 110 was used, with k=1, x_{cl}=0.84. Since neither k nor x_{cl} has been determined experimentally, the location and height of the cliff are given for illustrative purposes only. Also the cliff is not expected to be sharp but should come in with a finite degree of abruptness, whose extent is not known. In the region of the "thud wall", the extra-extra push rises to very high values.

an effective centrifugal potential, proportional to L^2 divided by twice an effective moment of inertia or, what comes to the same thing, a centrifugal potential equal to the square of an effective angular momentum, $(fL)^2$, divided by twice the standard moment of inertia $M_r (R_1 + R_2)^2$, appropriate for approaching spheres just before contact. Here f is an "effective angular momentum fraction" [11]. The generalized formula for E_χ may then be written as follows:

$$\begin{aligned} E_\chi &= 0 \,, && \text{for } \zeta_e(l) \leqq \zeta_{th} \\ E_\chi &= K\left[\zeta_e(l) - \zeta_{th}\right]^2 \,, && \text{for } \zeta_e(l) > \zeta_{th} \,, \end{aligned} \tag{118}$$

where

$$\zeta_e(l) = \zeta_e + (fl/l_{ch})^2 \,. \tag{119}$$

Here $\zeta_e(l)$ is a generalized effective fissility and l/l_{ch} [equal to $(L/\hbar)/(L_{ch}/\hbar)$] is the total angular momentum quantum number in units of a characteristic angular momentum quantum number of the system I_{ch}, given by

$$I_{ch} = \frac{e\sqrt{mr_0}}{2\hbar} \frac{A_1^{2/3} A_2^{2/3} \left(A_1^{1/3} A_2^{1/3}\right)}{\sqrt{A}} = 0.10270 \frac{A_1^{2/3} A_2^{2/3} \left(A_1^{1/3} A_2^{1/3}\right)}{\sqrt{A}} \,. \tag{120}$$

An empirical value of the angular momentum fraction $f \approx \frac{3}{4} \pm 10\%$, was deduced in Ref. [5]. [It appears to be consistent with recent theoretical estimates, $f \approx 0.85 \pm 0.02$].

The problem of generalizing the extra-extra push to include angular momentum is more difficult, since a simple trading of centrifugal for electrostatic forces becomes questionable in the mononuclear regime. In particular, when the nuclear shape approaches the sphere, there is a qualitative difference between the electric potential, which stationary for the sphere and the centrifugal potential, which is not. The use of a *constant* angular momentum fraction is thus certainly not valid. An angular momentum *function* f_m that is made to depend on the fissility parameter χ might have more validity. The generalized mean fissility $\zeta_m(l)$ and the generalized mean fissility parameter $\chi_m(l)$ would then have the following appearances:

$$\zeta_m(l) = \zeta_m + (f_m l/l_{ch})^2 \,, \tag{121}$$

$$\chi_m(l) = \chi_m + (f_m l/l_{ch})^2 / \zeta_{crit} \,. \tag{122}$$

One has also tried a certain prescription for f_m involving a generalized, angular-momentum-dependent fissility parameter $\chi(l)$ in the mononuclear regime, defined by

$$\chi(l) = \chi + \eta(\chi)\, y \,,$$

where $\eta(\chi)$ was a certain function of χ, and y is the standard rotational parameter of fission theory [Ref. [15]], proportional to the square of the angular momentum, and given by

$$y \equiv \frac{(rotational\, energy\, of\, rigid\, sphere)}{(surface\, energy\, of\, sphere)} = \frac{L^2 \frac{4}{5} M R^2}{4\pi R^2 \gamma} \tag{123}$$

On the further examination, the definition of f_m in terms of the chosen $\eta(\chi)$ turned out be unsatisfactory (f_m did not reduce to f for symmetric systems) and in what follows we shall revert to using one and the same constant angular momentum fraction f in the dinuclear and mononuclear regimes. This is not a satisfactory solution of the problem, but at least it is a simple prescription that does not hide its shortcomings in elaborate algebra. It may be good enough to illustrate the qualitative features associated with the existence of an extra-extra push.

$$E_{\chi\chi} = E_\chi\,, \qquad \text{for } \zeta_m(I) \leqq \zeta_{cl}\,, \tag{124}$$

$$E_{\chi\chi} = K\left[\zeta_m(l) - \zeta_m\right]^2 \quad \text{for } \zeta_m(l) > \zeta_{cl}\,, \tag{125}$$

where $\zeta_m(l)$ is given by Eq. 125 with $f_m = f$.

Note that, with f_m taken equal to f, no new adjustable parameters have been introduced in our scheme of estimating the extra-extra push in the presence of angular momentum. This is just as well, since this aspect of the theory is so uncertain that it would be foolish to hide its anticipated shortcoming by the adjustment of an arbitrary and possibly unphysical parameter.

According to the extra push theorem of Ref. [5], conservation of energy and angular momentum leads to the following relation between the center-of-mass energy E and the cross section σ (equal to πb^2, where b is the largest contributing in-pact parameter) for a process that demands for its inception an extra radial injection energy containing a contribution from the centrifugal repulsion, assumed to be proportional to the square of the angular momentum:

$$\sqrt{E - B - \frac{\sigma E}{\pi r^2}} = \alpha + \beta \frac{\sigma E}{\pi r^2} + \ldots\,. \tag{126}$$

Here B is the potential energy and r the center separation at contact. The quantities α, β are constants for a given colliding system. Eq. 130 follows by inspection from the (square root of) the energy conservation equation: the left-hand side is the square root of the energy available for radial motion at contact (because $\sigma E/\pi r^2$, equal to $b^2 E/r^2$, equal to $L^2/2M_r r^2$, is the orbital energy) and is thus equal to the square root of the extra or extra-extra push. The right-hand side is a way of writing this quantity (proportional to the extra injection *velocity* at constact) as consisting of an L-independent part and a centrifugal part, proportional to L^2 ($\sigma E/\pi r^2$ is proportional to L^2, see above). If Eqs. 109 and 110 are used for E_χ and $E_{\chi\chi}$, the constants α and

β are found to be given by

$$\begin{aligned} \alpha_\chi &= \sqrt{K\left(\zeta_e - \zeta_{th}\right)}, \qquad & \alpha_{\chi\chi} &= \sqrt{K\left(\zeta_m - \zeta_{th}\right)}\ , \\ \beta_\chi &= \frac{8\sqrt{K}}{e^2/r_0}\frac{f^2}{A_1^{\frac{1}{3}}A_2^{\frac{1}{3}}}, & \beta_{\chi\chi} &= \frac{8\sqrt{K}}{e^2/r_0}\frac{f_m^2}{A_1^{\frac{1}{3}}A_2^{\frac{1}{3}}}\ , \end{aligned} \tag{127}$$

the suffixes χ or $\chi\chi$ referring to the extra or extra-extra push, respectively.

The solution of the quadratic equation 126 is

$$\sigma = \frac{\pi r^2}{E}\left[\sqrt{\left(\frac{\alpha\beta+\frac{1}{2}}{\beta^2}\right)^2 - \left(\frac{\alpha^2+\beta-E}{\beta^2}\right)} - \left(\frac{\alpha\beta+\frac{1}{2}}{\beta^2}\right)\right] \tag{128}$$

and gives explicitly the energy-dependence of the cross section for a process requiring for its initiation a certain additional radial energy over the interaction barrier. The above cross section is the TOTAL fusion cross section of two heavy nuclei.To actually calculate the formation cross section of the compound nucleus which would survive the following fission process we have to utilize a different expression based on the Glas-Mosel idea of multiplying the fusion transmission (tunneling) by a fission survival probability.This we do in the next sub-section.

Fig. 12(a) illustrates the nature of the excitation functions predicted by Eq. 128. The solid curve is the cut-off value of πb^2 above which the two idealized nuclei do not touch, as given by the standard formula

$$\sigma = \pi b^2 = \pi r^2\left(1 - \frac{B}{E}\right)\ , \tag{129}$$

obtained by setting to zero the right-hand side of Eq. 127 (no extra push). For impact parameters b above the solid curve, the collisions are dominated by elastic scattering. (In a more refined model that takes into account the diffuseness of the nuclear surfaces, quasi-elastic events would appear for b values just above the solid curve). Thus the solid curve gives approximately the reaction cross section. The dashed curve in 12(a) gives the value of πb^2 below which the extra push in the radial direction has been exceeded, the conditional saddle has been overcome, and fusion has taken place in the sense of the formation of a mononucleus. The area between the solid and dashed curves corresponds, therefore, to dinucleus (deep-inelastic) reactions. The dotted curve corresponds to the locus of impact parameters above which the schematic model (with nominal parameters) suggests that the spherical shape would not be attained (because of the entrance-channel, extra-extra push limitation) and a mononucleus (fast-fission) reaction would be expected. (The dotted curve was drawn using Eqs. 128, 129 for the extra-extra push, with $k = 1$, $\chi_{cl} = 0.84$ and $f_m = 0.75$. Since none of the relevant quantities, k, $_{cl}$, f_m, is well known, the dotted curve is shown for illustrative purposes only, and it should not be taken as a quantitative

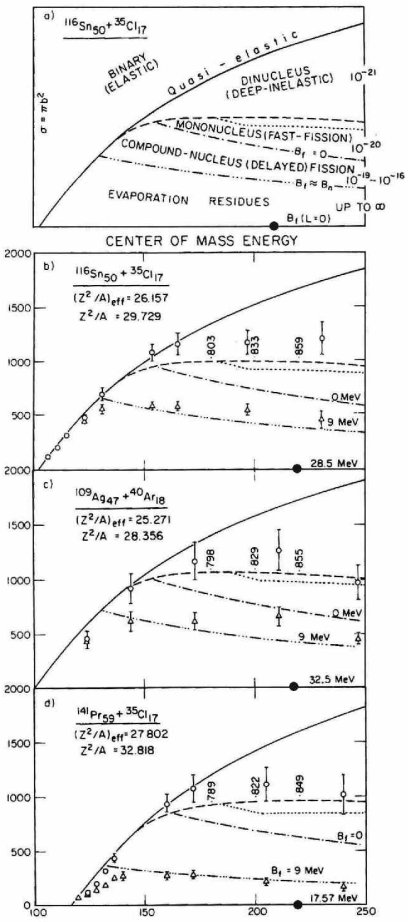

Figure 12 The excitation functions for various types of reactions. Fig. a. illustrates the qualitative distinction between binary (elastic and quasi-elastic) reactions, dinucleus (deep inelastic) reactions, mononucleus (fast-fission) reactions, and compound nucleus reactions. The latter divide into (delayed) fission reactions and evaporation residue reactions. Some characteristic lifetimes (in seconds) are indicated on the right. The dotted curve illustrates qualitatively the additional entrance-channel limitation on compound-nucleus formation resulting from the requirement of an extra-extra push to reach the vicinity of the spherical shape. Figs. b, c, d show a comparison of theory and experiment for three cases. The triangles refer to evaporation-residue cross sections, to be compared with the triple-dot-dashed curves. The circles have had cross sections for fission-like events added and are to be compared with the dashed curves. There are considerable uncertainties in both theory and measurement. In particular, the distinction between deep-inelastic and fission-like events in expected to become blurred at the higher energies, and the dashed curves should be imagined as fading out towards the right. The labels along the dashed curves refer to the generalized fissility parameter $\chi_e\,(l)$. The labels $B_f = 0$, $B_f \approx B_n$, $B_f\,(L = 0)$ refer to loci along which the fission barrier (of a rotating, idealized drop) has the value zero, or is about equal to the neutron binding energy, or has its full value corresponding to zero angular momentum.

prediction of the theory). The schematic model suggests that below the dotted curve the vicinity of the spherical shape might be attained. This still does not mean that a compound nucleus would be formed since, for this to be the case, there should be present a finite barrier against redisintegration. In the example illustrated in 12(a), this might actually not be the case: the dot-dashed curve shows the locus of impact parameters along which the fission barrier, calculated according to the rotating liquid drop model, has vanished (see appendix). Thus *all* of the region between the dashed and dot-dashed curves would correspond to mononucleus (fast-fission) reactions. Below the dot-dashed curve a finite fission barrier begins to grow, increasing in proportion to the distance below the critical locus (labeled $B_f = 0$). Reactions captured inside the potential-energy hollow defined by this barrier will not disintegrate until after a certain time delay, which the system requires to find its way out of the hollow. According to the statistical theory of rate processes, the lengthening of the fission lifetime is expected to be, roughly, by a factor involving the exponential of the fission barrier divided by the relevant nuclear temperature at the saddle point for fission. For finite temperatures the fission lifetimes are, therefore, not expected to change suddenly as the reaction moves into the region below the dot-dashed curve. In fact, the transition should be quite gradual. When, however, the fission barrier has grown sufficiently, the lengthening of the lifetime should become drastic (exponentially) and may, in typical cases, amount to several powers of ten if the temperature is a fraction of an MeV, but only one or two powers of ten (or less) for temperatures of several MeV. The decay of the compound nucleus by fission, after the above time delay, is expected to dominate when the fission barrier is less than the barrier against particle emission, most often (but not exclusively) neutron emission. The triplet dot-dashed curve in Fig. 5a shows the locus along which the fission barrier of the rotating liquid drop has reached the value B_n, the neutron binding energy. Below about this locus the decay of the compound nucleus should be dominated by particle (neutron) evaporation, leading to evaporation residues rather than fission fragments as the final products of the reaction. The lifetimes of these evaporation residues (after further deexcitation) may be very long, being governed by the relevant α-and β-decay or spontaneous-fission lifetimes. Illustrative orders of magnitude of the different characteristic lifetimes are noted on the right of Fig. 12(a). The abscissa itself in Fig. 12(a) corresponds to the locus of zero impact parameters (head-on collisions), where the fission barrier has attained its maximum height, corresponding to a system with no angular momentum, as indicated by the label $B_f\,(L = 0)$.

The theoretical curves in Fig. 12(a) (representing the reaction $^{116}Sn +^{35} Cl$, with a combined atomic number $Z = 67$)were constructed using the formulae explained above, and using the following values of the parameters: $\chi_{th} = 0.70$, $a = 12$, $f = \frac{3}{4}$. [These are the values deduced from a fit to the fusion data of Ref. [16], involving heavier systems in the atomic number range $Z = 94 - 110$. A comparison with experimental data [12] is shown in 12(b). The triangles are measured evaporation-

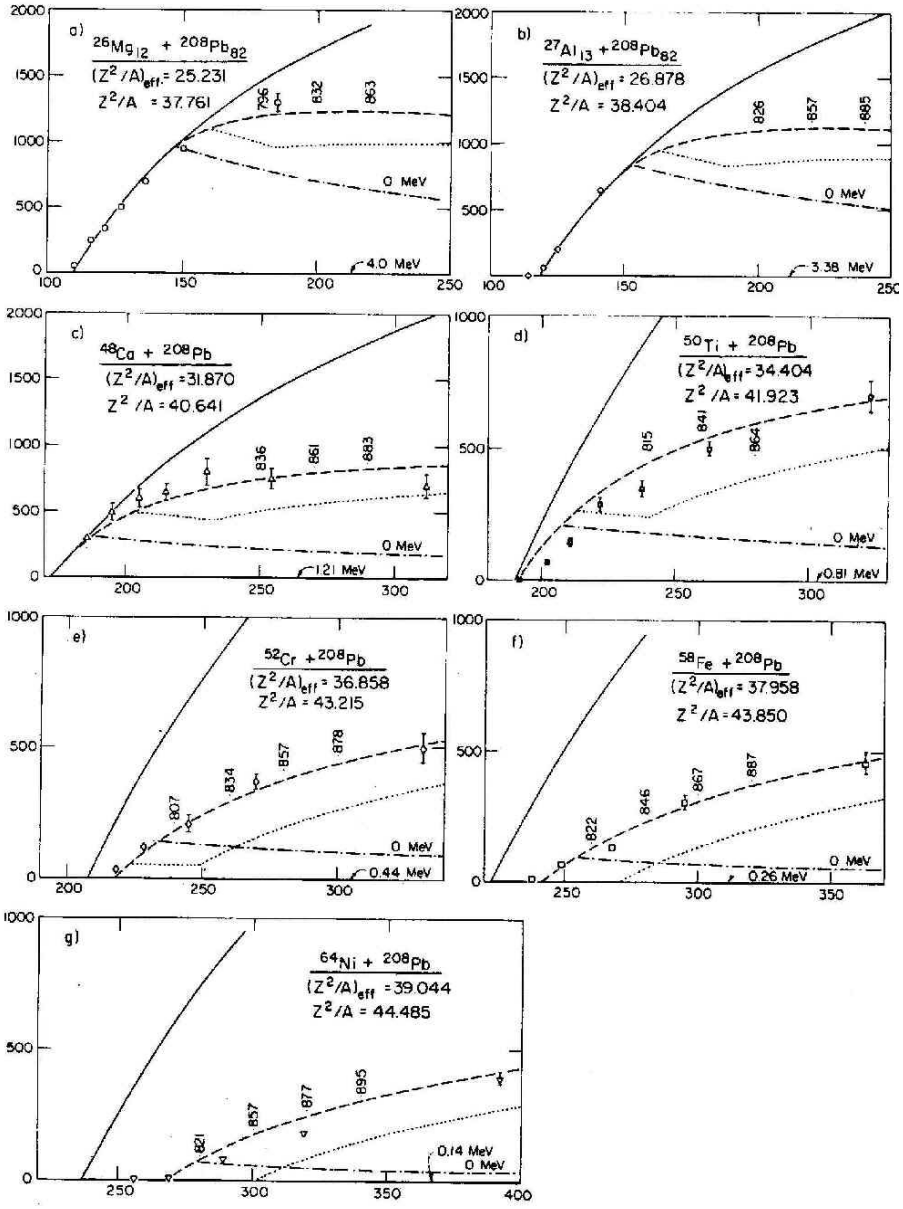

Figure 13 This is like Fig. 12, but for a set of seven reactions with heavier systems. The parameters of the theory($x_{th} - 0.70 \pm 0.02,\ a = 12 \pm 2,\ f = 0.75 \pm 10\%$) were fitted to these data and used without modification in (I). The dotted curves, corresponding to the entrance-channel, extra-extra push limitation, are for illustrative purposes only.

residue cross sections, and the circles are sums of evaporation residues and fission-like events. An approximate correspondence with the triple dot-dashes and dashed curves is evident. Fig. 12(c) makes a similar comparison with the slightly lighter system $^{109}Ag +^{40} Ar(Z = 65)$ and Fig. 12(d) with $^{141}Pr +^{35} Cl(Z = 86)$. Considering the uncertainties of the measurements there does not appear to be evidence for a serious disagreement at this stage, but the fact that the fusion cross sections (the circled points) are systematically higher than the calculated dashed curves may be significant. [Compare Ref. [12])].

Fig. 13(a-g) provide essentially the same confrontation of theory and experiment as Refs.[5, 11, 16], except that the calculated curves are now based on using the parameter $\chi_{th} = 0.70$ rather than $(Z^2/A)_{th} = 33$ to define the threshold fissility. Note the small three-digit numbers appearing above the dashed curves in Figs. 12 and 13. They give the values of $\chi_e\,(l)$ along these curves as function of bombarding energy. At the critical energy where the dashed curve peels off from the solid curve the corresponding label would be 0.70, the value of χ_{th}. We see that in the energy range displayed , the values of $\chi_e\,(l)$ soon exceed 0.8. Since (for symmetric systems) $\chi \approx 0.8$ marks the point where the saddle-point shape loses its neck constriction (and becomes convex everywhere for $\chi \gtrsim 0.8$), one might have expected that the physical significance of the conditional saddle-point shape would be lost beyond $\chi_e\,(l) \approx 0.8$. The distinction between deep-inelastic and fast-fission reactions should then be more and more difficult to maintain. (Thus the dashed curves ought to have been made to fade out towards the right, so that the deep-inelastic and fast-fission reactions would merge at high energies). Note also that for the heavier systems in Fig. 12 the predicted need for an extra-extra push could be playing an increasingly important role. For example, in the case of $^{208}Pb +^{52} Cr$, the entrance-channel limitation on compound-nucleus formation, related to the cliff in Fig. 10 and resulting in the dotted curve in Fig. 12(d), dips significantly below the dot-dashed curve and in Figs. 13(f) and **??**(II-g) there is finally a need for an extra-extra push to form a compound nucleus even in head-on collisions. Two things should, however, be kept in mind. First, the location of the dotted curves depends on the parameters χ_{cl} and k and the function f_m, whose values are unknown. (The values $\chi_{cl} = 0.84$, $k = 1$, chosen for purposes of illustration, should not be allowed to acquire the status of a theoretical prediction). Second, by the time the dotted curves in Figs. 13(e-g) become a more serious limitation on compound-nucleus formation than the dot-dashed curves, the fission barriers, even for head-on collisions, are only a fraction of an MeV. Thus, the extra-extra push entrance-channel limitation would be almost academic. The entrance-channel limitation might conceivably be more relevant when the compound nucleus is stabilized by a shell effect. In such cases the barrier against fission might be several MeV but the requirement of an extra-extra push might prevent the system from reaching the vicinity of the spherical shape, where the shell effect would have a chance to manifest itself.

A confrontation of the present theory with experiments on compound nucleus formation cross section is becoming possible through the analysis of evaporation-residue measurements. A particularly relevant set of experimental "effective barriers" for the formation of compound nuclei has been presented in Ref. [17]. These are barriers that would have to be inserted in conventional calculations of evaporation-residue cross sections in order to reproduce the observed cross sections for various (χn) reactions following the collision of two nuclei. By comparing such barriers with standard interaction barriers (either measured directly or calculated by an adequate semi-empirical procedure fitted to measurements throughout the lighter part of the periodic table) one may look for anomalies (in the case of heavy reacting systems) that would signal the need for an extra or extra-extra push. Table 2, based on Refs. [**?**, 18], lists six barrier estimated semi-empirically. [These estimates were made by lowering by 4% theoretical barriers obtained by combing the nuclear proximity potential with the Coulomb interaction between two (point) charges; see Ref. [18]].

Reaction	$B_{\rm exp}$*	$0.96B_{prox}$	$B_{\rm exp} - 0.96B_{prox}$	$\Delta B_{theory} = 0$, or $k\,(\zeta_e - \zeta_{th})^2$	$\zeta_e - \zeta_{th}$
$^{40}Ar_{18} + ^{206}Pb_{82}$	162±3	158.95	3.05±3	0	-2.0545
$^{50}Ti_{22} + ^{208}Pb_{82}$	191±3	190.14	0.86±3	1.17	1.1703
$^{50}Ti_{22} + ^{208}Bi_{83}$	190±3	192.38	-2.38±3	1.65	1.3874
$^{86}Kr_{36} + ^{123}Sb_{51}$	209.4±3	197.77	11.63±3	3.29	1.8018
$^{94}Zr_{40} + ^{124}Sn_{50}$	219.3±3	213.00	6.30±3	11.41	3.3214
$^{76}Ge_{32} + ^{170}Er_{68}$	$242^{+\infty}_{-5}$	227.00	$15.00^{+\infty}_{-5}$	20.63	4.5475
$^{86}Kr_{36} + ^{160}Gd_{64}$	≥ 260	239.30	≥ 20.70	33.27	5.6755
$^{110}Pd_{46} + ^{136}Xe_{54}$	≥ 283	256.45	≥ 26.55	56.00	7.1944

*Ref. [30]).

TABLE 2 - Experimental and theoretical interaction barriers

As regards the existence of a cliff, the data are consistent with a position of the cliff near to or above the $^{86}Kr + ^{160}Gd$point, for which the value ofζ_g is 39.9 and the value of χ_m is 0.835. The $^{209}Bi + ^{54}Cr$ reaction with $\chi_m = 0.829$ also appears to be below the cliff; see the following section. Thus we deduce tentatively that $\chi_{cl} \gtrsim 0.84$, $(Z^2/A)_{cl} \gtrsim 40$ in round numbers. Experimental evidence allowing an estimate of an upper limit for χ_{cl} is even more uncertain, but one might argue as follows. It may be expected that angular distributions of the fission fragments from compound nucleus reactions will be forward-backward symmetric, because the compound system makes many revolutions as it decays. Conversely, a fast-fission reaction may take place in a time less than required for one-half revolution and could, therefore, result in an angular distribution intermediate between the compound-nucleus type and the strongly focused, deep-inelastic type. As an example, the reaction $^{50}Ti + ^{208}Pb$ with $\chi_m = 0.79$ is found to be of the compound nucleus type, when the bombarding energy

is close to the barrier and the contributing l-values are below $40\hbar$, Ref. [16]. On the other hand, the $^{56}Fe + ^{208}Pb$ reaction with $\chi_m = 0.858$ $((Z^2/A)_m = 41.1)$ (Z^2/A) gives rise to forward-backward asymmetric angular distributions of the fast type at all bombarding energies including the lowest, where the maximum contributing l-value is about 30 $\hbar$, ref [19]. From these two experiments one might estimate that χ_{cl} should lie between 0.79 and 0.86. It should be stressed that this interpretation of the experiments not unambiguous. The noncompound features found with the $^{56}Fe + ^{208}Pb$ reactions could be due to interference from tails of the deep inelastic angular and mass distributions. thus obscuring an underlying reaction with perfect compound equilibrium properties. (Such interferences would be less pronounced in the case of the $^{50}Ti + ^{208}Pb$ reaction, because the symmetric mass yields are higher here). In any case, the value $\chi_{cl} = 0.84$ used for illustrative purposes in preparing Figs. 12-13, is consistent with the tentative lower limit $\chi_{cl} \gtrsim 0.84$ and with the hypothetical upper limit $\chi_{cl} \lesssim 0.86$.

7 Formation cross section

The formation cross section of a very heavy nucleus produced after the evaporation of one neutron reads

$$\sigma_{1n}(E_{HI}) = \pi\overline{\lambda}^2 \sum_{l=0}^{l_{\max}} (2l+1)\ T_l(E_{HI})\ P_{1n,l}(E^*), \tag{130}$$

where E_{HI} is the optimal bombarding energy in the center-of-mass system (the energy corresponding to the maximum of the excitation function), $E^* = E_{HI} - Q$ is the optimal excitation energy, Q is the Q-value for a given reaction, $\overline{\lambda} = \sqrt{\hbar^2/(2\mu E_{HI})}$ is the reduced de Broglie wave-length of the projectile and μ is the reduced mass. The quantities $T_l(E_{HI})$ and $P_{1n,l}(E^*)$ are the transmission probability through the fusion barrier and the survival probability of the compound nucleus (the neutron-to-total-width-ratio) for a given l. We terminate the summation in Eq.(130) at angular momentum l_{max} for which the contribution to σ_{1n} becomes smaller than 1%.

The above formula is similar to the Glas-Mosel formula,(104). Note that within the Bjornholm-Swiatecki model,the expression for the cross section is given by a similar expression as Eq.(130).

Transmission probability through the fusion barrier $T_l(E_{HI})$ is calculated by means of the WKB approximation,

$$T_l(E_{HI}) = \frac{1}{1 + \exp(2S_l(E_{HI}))} \tag{13.56}$$

Since we deal with low angular momenta ($l_{max} = 26 - 30$) and thin fusion barriers ($1.35 - 1.65$ fm), the action integral $S_l(E_{HI})$ between the barrier entrance and exit points for a given angular momentum l may be expressed by the action integral for

zero angular momentum,

$$S_l(E_{HI}) \approx S_0(E_{HI} - E_{centr}(R)), \tag{13.57}$$

where $E_{centr}(R) = [\hbar^2 l(l+1)]/[2\mu R^2]$ is the centrifugal energy at a certain distance R connected with the position of the fusion barrier.

For the sake of simplicity, we calculate the action integral assuming the most likely fusion barrier V_{fu} instead of considering the barrier distribution. We approximate the fusion barrier V_{fu} around its top by the inverted parabola,

$$V_{fu}(r) = B_{fu} - q(r - R_{fu})^2, \tag{13.58}$$

where r is the distance between the centers of the reaction partners. The position of the top of the fusion barrier R_{fu} and the barrier height B_{fu}, as well as the coefficient q describing the curvature of the barrier, are dependent on the combination of the colliding nuclei.

We parametrize the quantity q by the formula

$$q = \frac{B_{fu} - Q}{d^2}, \tag{13.59}$$

where $d = 1$ fm is taken, which corresponds to the barrier thickness of $1.35 - 1.65$ fm. Within this parametrization, we obtain the numerical value of q equal to the height of the fusion barrier relative to the ground state of the compound nucleus, which leads to a good reproduction of the measured formation cross sections [20, 21, 22, 23], as shown in Table 1.

The height of the fusion barrier

$$B_{fu} = \frac{Z_T Z_P e^2}{R_e} \tag{13.60}$$

is expressed by the Coulomb energy at an effective distance R_e. The latter is strongly dependent on atomic number of the target, Z_T, and the projectile, Z_P, which was observed experimentally [24] and theoretically [25]. Here, e is the elementary electric charge. We obtain the expression for the quantitity R_e assuming that the difference between R_e and the distance R_{12} at which the colliding nuclei are at contact is inversely proportional to the height of the fusion barrier. After simple algebra, we obtain the formula

$$R_e = \frac{R_{12}}{1 - c/Z_T Z_P} > R_{fu} > R_{12}, \tag{13.61}$$

where c is the model parameter controlling the height of the fusion barrier. The distance R_{12} at which the colliding nuclei are at contact is the sum of the half-density radii of the target and the projectile and is given by

$$R_{12} = c_T R_T + c_P R_P. \tag{13.62}$$

Here, R_T and R_P are the nuclear radii of the target and the projectile determined from the root-mean-square-charge-radii, and c_T and c_P are the coefficients relating R_T and R_P with the half-density radii of the target and the projectile, respectively. The radii R_T and R_P are calculated by using the Nerlo-Pomorska and Pomorski formula [26],

$$R_T = 1.256\ (1 - 0.202\ \frac{N_T - Z_T}{A_T})\ A_T^{1/3}, \qquad R_P = 1.256\ (1 - 0.202\ \frac{N_P - Z_P}{A_P})\ A_P^{1/3}. \tag{13.63}$$

For the projectiles with $Z_P < 38$,

$$R_P = 1.240\ (1 + \frac{1.646}{A_P} - 0.191\ \frac{N_P - Z_P}{A_P})\ A_P^{1/3}, \tag{13.64}$$

where A_T and N_T are mass and neutron numbers of the target and A_P and N_P are the same quantities for the projectile. The coefficients c_T and c_P relating R_T and R_P with the half-density radii may be deduced from Ref.[27] and are specified in Ref.[28] (Eq.(9) therein). The model parameter $c = 352.93548$ is fixed to reproduce the cross section of ^{208}Pb(^{50}Ti,1n)^{257}Rf at the maximum of the measured excitation function [29]. The choice of this reaction is motivated by the fact that the nice measurement of the excitation function for ^{257}Rf was performed at GSI-Darmstadt [29].

The action integral calculated for the fusion barrier introduced above is given by

$$S_l(E_{HI}) \approx \frac{\pi}{2}\sqrt{\frac{2\mu}{\hbar^2 q}}[B_{fu} + E_{centr}(R) - E_{HI}], \tag{13.65}$$

where $R = (R_{12} + R_e)/2$ is taken.

Using empirical formulas for the Coulomb barrier for proton emission and α-particle emission given in Ref.[30], as well as proton-separation and α-decay energies which may be calculated in the macroscopic-microscopic model [31, 32, 33], we are able to determine thresholds for proton and α-particle evaporation. Since for the compound nuclei in question the calculated thresholds for proton and α-particle evaporation are higher than that for neutron emission, one can express the survival probability of the compound nucleus (the neutron-to-total-width-ratio) for a given angular momentum l only by the neutron-to-fission-width-ratio $(\Gamma_n/\Gamma_f)_l$,

$$P_{1n,l} \approx \frac{(\Gamma_n/\Gamma_f)_l}{1 + (\Gamma_n/\Gamma_f)_l}\ . \tag{13.66}$$

Both widths are dependent on the density of single-particle and collective energy-levels. For low excitations in question ($E^* \lesssim 15$ MeV), shell effects are still present leading to lower level density in the equilibrium configuration $\rho_{eq}(E^*)$ than that in the saddle-point configuration $\rho_{sd}(E^*)$. Lower level density in the equilibrium configuration should lead to slower neutron emission in comparison with fission also for nuclei with comparable thresholds for both processes. The excitation-energy dependence of

the neutron-to-total-width-ratio measured for heavy actinides at Joint Institute for Nuclear Research in Dubna [34] may be explained in this way for low excitations. Using the statistical model formula for the Fermi gas, in which thermal damping of shell effects was introduced through the level density parameters, one obtaines values for the neutron-to-fission-width-ratio $(\Gamma_n/\Gamma_f)_0$ significantly smaller than 10^{-4} for many very heavy compound nuclei [28, 35]. Those values correspond to large times for neutron evaporation allowing deexcitation of the compound nucleus by γ emission. The latter process, however, is not observed for the very heavy compound nuclei. Therefore, in the present study, we use a different method for calculating $(\Gamma_n/\Gamma_f)_l$. Instead of describing $(\Gamma_n/\Gamma_f)_l$ by the formula for the Fermi gas with inserted different level-density parameters for the equilibrium configuration of $1n$-evaporation residue and for the saddle-point configuration of the compound nucleus, we use a constant temperature formula for $(\Gamma_n/\Gamma_f)_l$ in which we insert different temperatures T_{eq} and $T_{sd} > T_{eq}$ for these configurations, respectively.

Assuming that the rotational energy is not available for neutron evaporation, as well as for fission, an expression for the neutron-to-fission-width-ratio reads

$$(\Gamma_n/\Gamma_f)_l = \frac{k_{eq}}{k_{sd}} \cdot kA^{2/3}T_{eq} \exp\left(\frac{B_f + \Delta_{sd}}{T_{sd}} - \left[\frac{\hbar^2 l(l+1)}{2J(eq)T_{eq}} - \frac{\hbar^2 l(l+1)}{2J(sd)T_{sd}}\right] - \frac{S_n + \Delta_{eq}}{T_{eq}}\right). \tag{131}$$

Here, k_{eq} and k_{sd} are the collective enhancement factors for the equilibrium and the saddle-point configurations, respectively. For the equilibrium configuration of $1n$-evaporation residue with the quadrupole deformation $\beta_2 > 0.15$ and for the saddle-point configuration of all compound nuclei, k_{eq} and k_{sd} equal to 100 [36] are used because of the presence of the rotational bands. This value is consistent with the recent measurements [37]. For spherical and transitional nuclei ($\beta_2 \leq 0.15$), $k_{eq} = 1$ is taken. The constant $k = 0.14$ MeV^{-1} is a coefficient obtained in the statistical model and A is mass number of the compound nucleus. The quantities B_f and S_n are the static fission-barrier height and the neutron-separation energy (thresholds for fission and neutron emission), while Δ_{sd} and Δ_{eq} are the energy shifts in the saddle-point of the compound nucleus and the equilibrium configuration of $1n$-evaporation residue, respectively. These energy shifts are used to take into account differences in level densities between even-even, odd and odd-odd nuclei [38]. Taking as the reference the potential energy surface of an odd nucleus [38], we use $\Delta_{eq} = 12/\sqrt{A}$, 0 and $-12/\sqrt{A}$, for even-even, odd and odd-odd $1n$-evaporation residue, respectively. The energy shift in the saddle-point configuration of the compound nucleus Δ_{sd} is significantly larger (see for instance Ref.[39]). In our calculation, the value of 1.5 MeV for even-even and 0 for odd compound nuclei is taken. The moments of inertia $J(eq)$ and $J(sd)$ for the equilibrium and the saddle-point deformations are assumed to be equal to those for the rigid body and are calculated taking advantage of the deformation dependence obtained in Ref.[40] and the nuclear radii given by the Nerlo-Pomorska and Pomorski formula [26].

The temperature in the equilibrium configuration of $1n$-evaporation residue

$T_{eq} = (\frac{d}{dE^*} ln \rho_{eq})^{-1}$ must be lower than the temperature in the saddle-point configuration of the compound nucleus T_{sd} because the level density $\rho_{eq}(E^*)$ increases faster with increasing excitation energy E^* in comparison with the level density in the saddle-point configuration of the compound nucleus $\rho_{sd}(E^*)$. The reason for this is thermal damping of the strong ground-state shell-effect. (In the saddle point, there is no shell effect or it is much weaker than in the equilibrium configuration.) The density of the lowest levels in a very heavy nucleus ($E^* \lesssim 3$ MeV) is well described by the constant temperature formula with the average temperature $T_{eq}^{low} = 0.4$ MeV [41]. Assuming $T_{eq} = (T_{eq}^{low} + T_{sd})/2 = 0.7$ MeV, we obtain $T_{sd} = 1$ MeV. Since the experimentally observed neutron-to-total-width-ratio is excitation-energy dependent, the constant temperature $T_{eq} = 0.7$ MeV may be used only for a narrow range of excitation energy around the maximum of the $1n$-channel excitation function for the heaviest nuclei. Within $T_{eq} = 0.7$ MeV and $T_{sd} = 1$ MeV, we obtain realistic values of the order of $10^{-4} - 10^{-1}$ for the $(\Gamma_n/\Gamma_f)_0$ ratio for the nuclei in question. For high excitations for which shell effects are fully damped, experimental data [34] may be well described by the standard statistical model formula for $(\Gamma_n/\Gamma_f)_l$ within equal temperatures.

Since for almost all nuclei in question, the calculated threshold for fission following neutron emission is lower and only for few of them comparable with the calculated threshold for two-neutron emission, we determine the optimal excitation energy which corresponds to the maximum of the excitation function as $E^* = S_n + B_f^{ER}$, where B_f^{ER} is the height of the static fission barrier for $1n$-evaporation residue. This excitation energy corresponds to the bombarding energy in the lab system given by

$$E_{lab} = (Q + S_n + B_f^{ER}) \frac{A_T + A_P}{A_T} \ . \tag{132}$$

This simple expression may be used because of the narrowness of the excitation function for the heaviest atomic nuclei.

Nuclear structure influences the formation cross section through the model input-quantities Q, S_n, B_f, B_f^{ER} and the equilibrium and saddle-point deformations. In order to obtain Q-values, we calculate masses of the compound nuclei by means of the macroscopic-microscopic model [31, 32, 33] and use measured masses of the targets and the projectiles [42]. All the other input quantities are calculated by using the macroscopic-microscopic model [31, 32, 33].

8 Comparison with experimental data

We compare the calculated formation cross sections with the measured ones [20, 21, 22, 23] in Table 3.

Reaction	σ_{1n}(nb)	σ_{1n}^{exp}(nb)
^{208}Pb(^{48}Ca,1n)^{255}No	590	260^{+30}_{-30}
^{209}Bi(^{48}Ca,1n)^{256}Lr	250	61^{+20}_{-20}
^{208}Pb(^{50}Ti,1n)^{257}Rf	10.4	$10.4^{+1.3}_{-1.3}$
^{209}Bi(^{50}Ti,1n)^{258}Db	6.1	$2.9^{+0.3}_{-0.3}$
^{208}Pb(^{54}Cr,1n)^{261}Sg	580	500^{+140}_{-140}
^{209}Bi(^{54}Cr,1n)^{262}Bh	390	240^{+240}_{-132}
^{207}Pb(^{58}Fe,1n)^{264}Hs	9.7	$8.8^{+16.0}_{-3.5}$
Reaction	σ_{1n}(pb)	σ_{1n}^{exp}(pb)
^{208}Pb(^{58}Fe,1n)^{265}Hs	37	67^{+17}_{-17}
^{209}Bi(^{58}Fe,1n)^{266}Mt	33	$7.4^{+4.8}_{-3.3}$
^{208}Pb(^{62}Ni,1n)^{269}110	2.0	$3.5^{+2.7}_{-1.8}$
^{208}Pb(^{64}Ni,1n)^{271}110	17	15^{+9}_{-6}
^{209}Bi(^{64}Ni,1n)^{272}111	13	$3.5^{+4.6}_{-2.3}$
^{208}Pb(^{70}Zn,1n)^{277}112	3.2	$1.0^{+1.3}_{-0.7}$
^{208}Pb(^{86}Kr,1n)^{293}118	5.9	$2.2^{+2.6}_{-0.8}$

Table 3. The comparison of the calculated formation cross section σ_{1n} with the measured one σ_{1n}^{exp} [20, 21, 22, 23] for transactinides and heavy actinides produced in cold fusion reactions with the emission of only one neutron. The systematic uncertainty of the measured formation cross sections is equal to a factor of 2 [21]. In Table I, the measured values for the formation cross section with only statistical errors are given. Model parameter $c = 352.93548$ is fixed to reproduce the cross section of ^{208}Pb(^{50}Ti,1n)^{257}Rf at the maximum of the measured excitation function [29].

The experimental cross sections of ^{207}Pb(^{50}Ti,1n)^{256}Rf, ^{207}Pb(^{54}Cr,1n)^{260}Sg and ^{207}Pb(^{58}Fe,1n)^{264}Hs given in Refs.[43, 44, 45] are not included because they were measured at excitation energy significantly higher than the optimal one. Instead, the cross section of ^{207}Pb(^{58}Fe,1n)^{264}Hs measured at the excitation energy $E^* = 12.9$ MeV is compared with the calculated value. The systematic uncertainty of the measured formation cross sections is equal to a factor of 2 [21]. In Table I, the measured values for the formation cross section with only statistical errors are given. The obtained results agree with the experimental data within a factor of 2.4, on average. The calculated formation cross section of 5.9 pb for ^{293}118 overestimates a value [22] reported by the LBNL-Berkeley group only by a factor of 2.7 (a value obtained in the original model [28] was by about 2 orders of magnitude larger).

The calculation of the cross section of the reactions ^{90,92,94,96}Zr(^{124}Sn,1n) ^{213,215,217,219}Th [46] carried out at GSI-Darmstadt is outside the scope of the present paper because it requires considerable extension of our model. For nuclei like ^{213,215,217,219}Th, fission is not that important (high fission barriers) and, therefore, the excitation functions are broader with their maxima shifted towards higher excitation energies of $20 - 30$ MeV. The extension of the model would have to contain a method of determining the optimal bombarding energy because Eq.132 is no longer

valid for broad excitation functions.

Reaction	E_{lab} (MeV)	T_0	$(\Gamma_n/\Gamma_f)_0$	σ_{1n}
^{207}Pb(^{50}Ti,1n)^{256}Rf	227.8	$1.2 \cdot 10^{-6}$	$1.7 \cdot 10^{-1}$	3.3 nb
^{208}Pb(^{50}Ti,1n)^{257}Rf	228.8	$3.0 \cdot 10^{-6}$	$2.2 \cdot 10^{-1}$	10.4 nb
^{207}Pb(^{54}Cr,1n)^{260}Sg	253.1	$1.7 \cdot 10^{-7}$	$6.6 \cdot 10^{-2}$	180 pb
^{208}Pb(^{54}Cr,1n)^{261}Sg	253.8	$3.9 \cdot 10^{-7}$	$9.6 \cdot 10^{-2}$	580 pb
^{207}Pb(^{58}Fe,1n)^{264}Hs	279.4	$3.3 \cdot 10^{-8}$	$2.0 \cdot 10^{-2}$	9.7 pb
^{208}Pb(^{58}Fe,1n)^{265}Hs	279.7	$6.6 \cdot 10^{-8}$	$3.8 \cdot 10^{-2}$	37 pb
^{207}Pb(^{62}Ni,1n)^{268}110	306.4	$6.9 \cdot 10^{-9}$	$4.0 \cdot 10^{-3}$	380 fb
^{208}Pb(^{62}Ni,1n)^{269}110	306.4	$1.2 \cdot 10^{-8}$	$1.2 \cdot 10^{-2}$	2.0 pb
^{207}Pb(^{64}Ni,1n)^{270}110	310.5	$1.9 \cdot 10^{-8}$	$1.1 \cdot 10^{-2}$	2.6 pb
^{208}Pb(^{64}Ni,1n)^{271}110	310.8	$3.9 \cdot 10^{-8}$	$3.3 \cdot 10^{-2}$	17 pb
^{207}Pb(^{68}Zn,1n)^{274}112	337.2	$3.0 \cdot 10^{-9}$	$1.0 \cdot 10^{-2}$	360 fb
^{208}Pb(^{68}Zn,1n)^{275}112	337.7	$7.2 \cdot 10^{-9}$	$1.5 \cdot 10^{-2}$	1.3 pb
^{207}Pb(^{70}Zn,1n)^{276}112	340.9	$5.1 \cdot 10^{-9}$	$1.6 \cdot 10^{-2}$	940 fb
^{208}Pb(^{70}Zn,1n)^{277}112	341.9	$1.6 \cdot 10^{-8}$	$1.8 \cdot 10^{-2}$	3.2 pb
^{208}Pb(^{74}Ge,1n)^{281}114	370.8	$5.3 \cdot 10^{-9}$	$6.0 \cdot 10^{-3}$	330 fb
^{207}Pb(^{76}Ge,1n)^{282}114	374.5	$4.4 \cdot 10^{-9}$	$4.5 \cdot 10^{-3}$	200 fb
^{208}Pb(^{76}Ge,1n)^{283}114	375.4	$1.4 \cdot 10^{-8}$	$6.6 \cdot 10^{-5}$	9 fb
^{208}Pb(^{82}Se,1n)^{289}116	412.3	$8.6 \cdot 10^{-8}$	$2.3 \cdot 10^{-4}$	190 fb

Table 4(a). The optimal bombarding energy in the lab system E_{lab}, the transmission probability through the fusion barrier for zero angular momentum T_0, the neutron-to-fission-width-ratio for zero angular momentum $(\Gamma_n/\Gamma_f)_0$ and the formation cross section σ_{1n} calculated for reactions based on ^{207}Pb and ^{208}Pb target nuclei. Reactions with stable projectiles are given on the left-hand side of the table and those with neutron-rich radioactive-ion-beams are placed on its right-hand side. In the calculation of $(\Gamma_n/\Gamma_f)_l$, the minimal fission barriers are used (in the original model [28, 35, 49], we used the fission-barrier heights B_f and B_f^{ER} for odd nuclei by 0.5 MeV higher because of the assumed specialization energy).

For excitations of $20 - 30$ MeV, the low temperature $T_{eq} = 0.7$ MeV cannot be used eighter. Moreover, evaporation of charged particles would have to be taken into account because of comparable thresholds for neutron evaporation and emission of charged particles. Furthermore, octupole deformation would have to be taken into account in the nuclear-structure-dependent input-quantities and in the moments of inertia. The calculation of the cross sections of lighter nuclei, like for example ^{179}Hg obtained in the cold fusion reaction ^{90}Zr(^{90}Zr,1n)^{179}Hg [47], would require also taking into account the γ-emission channel which competes with evaporation of the neutron and the charged particles. The results for the reactions based on ^{207}Pb and ^{208}Pb target nuclei are listed in Tables 4(a) and 4(b).

The calculated formation cross sections for transitional and spherical nuclei, i.e. for nuclei heavier than $^{282}114$, are smaller than the values obtained in Refs.[28, 35] mainly because of thicker fusion barrier in comparison with the cutoff Coulomb barrier used in the original model [28, 35]. The formation cross section decreases with increasing atomic number due to decreasing both the transmission probability through the fusion barrier and the neutron-to-fission-width-ratio. (In the original model, this decrease was mainly due to decreasing Γ_n/Γ_f). The reversal of this trend in our quantal model and the increase of the cross section of ^{208}Pb(^{86}Kr,$1n$)$^{293}118$ and ^{207}Pb(^{86}Kr,$1n$)$^{292}118$ is caused by the magicity of ^{86}Kr projectile ($N_P = 50$), which leads to larger Q-value and, consequently, to lower effective fusion barrier with larger transmission probability. This effect is not present in the dinuclear-system model exploited by the authors of Ref.[48], who describe the formation of the compound nucleus classically and predict a very small cross section of 5 fb [48] for the reaction ^{208}Pb(^{86}Kr,$1n$)$^{293}118$.

Reaction	E_{lab} (MeV)	T_0	$(\Gamma_n/\Gamma_f)_0$	σ_{1n}
^{208}Pb(^{84}Kr,$1n$)$^{291}118$	441.0	$7.4 \cdot 10^{-8}$	$2.0 \cdot 10^{-4}$	140 fb
^{207}Pb(^{86}Kr,$1n$)$^{292}118$	447.8	$3.7 \cdot 10^{-7}$	$2.0 \cdot 10^{-4}$	640 fb
^{208}Pb(^{86}Kr,$1n$)$^{293}118$	448.4	$1.2 \cdot 10^{-6}$	$5.7 \cdot 10^{-4}$	5.9 pb
^{208}Pb(^{80}Ge,$1n$)$^{287}114$	381.8	$3.7 \cdot 10^{-8}$	$2.4 \cdot 10^{-4}$	91 fb
^{207}Pb(^{82}Ge,$1n$)$^{288}114$	382.4	$9.5 \cdot 10^{-9}$	$2.3 \cdot 10^{-4}$	23 fb
^{208}Pb(^{82}Ge,$1n$)$^{289}114$	384.1	$4.6 \cdot 10^{-8}$	$8.7 \cdot 10^{-4}$	400 fb
^{207}Pb(^{84}Se,$1n$)$^{290}116$	415.8	$8.1 \cdot 10^{-8}$	$2.2 \cdot 10^{-4}$	160 fb
^{208}Pb(^{84}Se,$1n$)$^{291}116$	416.9	$3.3 \cdot 10^{-7}$	$7.8 \cdot 10^{-4}$	2.4 pb
^{207}Pb(^{86}Se,$1n$)$^{292}116$	415.5	$2.8 \cdot 10^{-8}$	$6.4 \cdot 10^{-4}$	170 fb
^{208}Pb(^{86}Se,$1n$)$^{293}116$	416.9	$1.2 \cdot 10^{-7}$	$2.0 \cdot 10^{-3}$	2.3 pb
^{207}Pb(^{88}Se,$1n$)$^{294}116$	413.8	$4.6 \cdot 10^{-9}$	$1.7 \cdot 10^{-3}$	77 fb
^{208}Pb(^{88}Se,$1n$)$^{295}116$	415.5	$2.3 \cdot 10^{-8}$	$4.4 \cdot 10^{-3}$	1.0 pb
^{207}Pb(^{88}Kr,$1n$)$^{294}118$	449.0	$2.1 \cdot 10^{-7}$	$5.1 \cdot 10^{-4}$	940 fb
^{208}Pb(^{88}Kr,$1n$)$^{295}118$	450.0	$8.5 \cdot 10^{-7}$	$1.2 \cdot 10^{-3}$	8.6 pb
^{207}Pb(^{90}Kr,$1n$)$^{296}118$	449.0	$6.5 \cdot 10^{-8}$	$9.6 \cdot 10^{-4}$	540 fb
^{208}Pb(^{90}Kr,$1n$)$^{297}118$	450.3	$2.9 \cdot 10^{-7}$	$2.1 \cdot 10^{-3}$	5.4 pb
^{207}Pb(^{92}Kr,$1n$)$^{298}118$	447.4	$9.2 \cdot 10^{-9}$	$2.0 \cdot 10^{-3}$	170 fb
^{208}Pb(^{92}Kr,$1n$)$^{299}118$	449.1	$4.9 \cdot 10^{-8}$	$3.2 \cdot 10^{-3}$	1.4 pb
^{208}Pb(^{92}Sr,$1n$)$^{299}120$	483.2	$5.2 \cdot 10^{-7}$	$8.3 \cdot 10^{-4}$	3.4 pb
^{207}Pb(^{94}Sr,$1n$)$^{300}120$	483.0	$4.8 \cdot 10^{-8}$	$8.1 \cdot 10^{-4}$	310 fb
^{208}Pb(^{94}Sr,$1n$)$^{301}120$	484.2	$2.2 \cdot 10^{-7}$	$1.2 \cdot 10^{-3}$	2.1 pb
^{207}Pb(^{96}Sr,$1n$)$^{302}120$	481.4	$5.3 \cdot 10^{-9}$	$1.2 \cdot 10^{-3}$	53 fb
^{208}Pb(^{96}Sr,$1n$)$^{303}120$	483.1	$3.0 \cdot 10^{-8}$	$1.4 \cdot 10^{-3}$	340 fb
^{207}Pb(^{98}Sr,$1n$)$^{304}120$	479.4	$5.0 \cdot 10^{-10}$	$1.7 \cdot 10^{-3}$	7 fb

Table 4(b). Continuation of Table 4(a).

In the present paper, we obtain the fusion-barrier heights by $1.3 - 3.3$ MeV larger than the heights of the cutoff Coulomb barrier calculated in Refs. [28, 35]. The parabolic barrier is thicker and, consequently, transmission probabilities of the order of $10^{-9} - 10^{-6}$ obtained in the present paper are much lower than those calculated in Refs. [28, 35]. The neutron-to-fission-width-ratio for zero angular momentum $(\Gamma_n/\Gamma_f)_0$ calculated by using Eq.131 is of the order of $10^{-4} - 10^{-1}$ for the compound nuclei in question. The values for the nuclear-structure-dependent quantities Q and S_n for reactions listed in Table 4 are given in Refs.[28, 35]. The values for the quantity B_f for even-even compound nuclei are also listed in Ref.[28]. In the present calculation, the fission-barrier heights for odd compound nuclei smaller by 0.5 MeV than those listed in Ref. [35] are used. This is because, in the calculation of $(\Gamma_n/\Gamma_f)_l$, the minimal fission-barrier heights B_f and B_f^{ER} for odd nuclear systems should be used. In the original model [28, 35, 49], we used higher B_f and B_f^{ER} for odd nuclei because of the assumed specialization energy of 0.5 MeV. The latter fission-barrier heights are more reliable for the description of the spontaneous fission rather than for the description of desintegration of the compound nucleus.

In the framework of the macroscopic-microscopic model [31, 32, 33], we predicted in Ref.[50] α-decay energies and half-lives for the nuclei in the decay chain of $^{293}118$. Later on, this decay chain was discussed by the other authors in Ref.[51] by using the Skyrme-Hartree-Fock-Bogoliubov method and in Ref.[52] in the relativistic-mean-field model. Again, in the framework of the macroscopic-microscopic model [31, 32, 33], we predicted α-decay chains which might be initiated by the nuclei $^{292}118$ and $^{294}119$ in Refs.[35, 50], respectively. In Ref.[35], we also discussed α-decay chains which might be initiated by $^{270}110$ and $^{276}112$.

Table 5 contains relatively large cross section calculated for the reactions which might lead to the transitional isotopes of undiscovered so far elements 119, 120 and 121.

Reaction	E_{lab} MeV	Q MeV	B_{fu} MeV	T_0 (10^{-6})	S_n MeV	B_f MeV	$(\Gamma_n/\Gamma_f)_0$ (10^{-4})	σ_{1n} (pb)
^{208}Pb(^{87}Rb,$1n$)^{294}119	462.9	313.47	339.37	1.1	8.00	5.45	3.0	2.7
^{209}Bi(^{86}Kr,$1n$)^{294}119	453.9	308.67	334.04	1.7	8.00	5.45	3.0	4.4
^{208}Pb(^{88}Sr,$1n$)^{295}120	478.6	323.14	350.06	0.61	8.25	5.34	3.1	1.6
^{209}Bi(^{88}Sr,$1n$)^{296}121	485.2	328.22	354.20	1.4	8.32	5.34	1.7	1.9
^{208}Pb(^{89}Y,$1n$)^{296}121	492.2	331.48	359.19	0.34	8.32	5.34	1.7	0.46

TABLE 5 -. In the table, the optimal bombarding energy E_{lab}, the Q-value, the height of the fusion barrier B_{fu}, the transmission probability through the fusion barrier for zero angular momentum T_0, the neutron-separation energy S_n and the static fission-barrier height B_f for the compound nucleus, the neutron-to-fission-width-ratio for zero angular momentum $(\Gamma_n/\Gamma_f)_0$ and the cross section σ_{1n} calculated for fusion reactions involving magic reaction partners which might lead to the synthesis of elements 119, 120 and 121.

In the calculation of $(\Gamma_n/\Gamma_f)_l$, the minimal (with no specialization energy) fission-barrier heights B_f and B_f^{ER} for odd and odd-odd nuclei are used.

This is again due to the magicity of the reaction partners, which leads to larger Q-value and, consequently, lower effective fusion barrier with larger transmission probability. In comparison with the previous study [49], we obtain the formation cross sections of $^{294}119$ by about 2 orders of magnitude smaller. For ^{208}Pb(^{87}Rb,1n)$^{294}119$, we predict the cross section of 2.7 pb which is by a factor of 1.6 smaller than that calculated for the reaction ^{209}Bi(^{86}Kr,1n)$^{294}119$ which might lead to the same isotope of element 119. The reason for this is larger effective fusion barrier for ^{208}Pb + ^{87}Rb in comparison with that for ^{209}Bi + ^{86}Kr. The predicted formation cross sections of 4.4 pb, 1.6 pb and 1.9 pb for ^{209}Bi(^{86}Kr,1n)$^{294}119$, ^{208}Pb(^{88}Sr,1n)$^{295}120$ and ^{209}Bi(^{88}Sr,1n)$^{296}121$, respectively, suggest a good chance for the synthesis of superheavy elements 119, 120 and 121 in these reactions.

Our results suggest that symmetric reactions involving magic nuclei might be carried out by using the present-day experimental technique. Although shell effects in the magic nuclei ^{124}Sn, ^{136}Xe, ^{138}Ba and ^{140}Ce are not as strong as in ^{208}Pb and ^{209}Bi, they act in both the target and the projectile and lead to the prediction of measurable cross sections of the reactions ^{136}Xe(^{124}Sn,1n)^{259}Rf, ^{136}Xe(^{136}Xe,1n)^{271}Hs, ^{138}Ba(^{136}Xe,1n)$^{273}110$ and ^{140}Ce(^{136}Xe,1n)$^{275}112$, which are collected in Table 6.

Reaction	E_{lab} MeV	Q MeV	B_{fu} MeV	T_0 (10^{-8})	S_n MeV	B_f MeV	$(\Gamma_n/\Gamma_f)_0$ (10^{-1})	σ_{1n} (pb)
^{136}Xe(^{124}Sn,1n)^{259}Rf	550.5	273.52	307.03	1.2	7.57	6.62	2.7	24
^{136}Xe(^{136}Xe,1n)^{271}Hs	628.4	300.63	329.58	9.5	7.06	5.88	2.7	170
^{138}Ba(^{136}Xe,1n)$^{273}110$	647.1	312.80	341.68	5.8	7.56	5.19	0.68	27
^{140}Ce(^{136}Xe,1n)$^{275}112$	664.9	324.71	353.68	2.8	8.09	4.42	0.15	2.9

TABLE 6. The same quantities as in Table III calculated for symmetric reactions based on magic reaction partners. In the calculation of $(\Gamma_n/\Gamma_f)_l$, the minimal (with no specialization energy) fission-barrier height B_f^{ER} for odd $1n$-evaporation residues is used. We obtain the cross section of 1.0 pb for ^{142}Ce(^{136}Xe,1n)$^{277}112$ (E_{lab} = 656.7 MeV). This means that the use of the heaviest stable isotope of cerium, ^{142}Ce, instead of magic ^{140}Ce, decreases the cross section by a factor of 2.9. Exchanging targets with projectiles leads to larger optimal bombarding energy. We obtain E_{lab} = 603.8 MeV, 656.6 MeV, 684.5 MeV and 685.7 MeV for ^{124}Sn(^{136}Xe,1n)^{259}Rf, ^{136}Xe(^{138}Ba,1n)$^{273}110$, ^{136}Xe(^{140}Ce,1n)$^{275}112$ and ^{136}Xe(^{142}Ce,1n)$^{277}112$, respectively. The values of the other quantities remain unchanged.

Some of these reactions might be more useful for producing deformed superheavy nuclei than the so called hot fusion reactions (very asymmetric reactions with the evaporation of several particles). For example, we predict the cross section of 27 pb for the symmetric reaction ^{138}Ba(^{136}Xe,1n)$^{273}110$ which might lead to the deformed nucleus $^{273}110$. The synthesis of this nucleus at JINR-Dubna in the hot fusion

reaction ^{244}Pu(^{34}S,5n)^{273}110 with the measured cross section of 0.4 pb has been reported in Ref.[**?**]. This value is almost 70 times smaller than that obtained in the present paper for ^{138}Ba(^{136}Xe,1n)^{273}110.

We predict that the most promising symmetric reaction for producing transactinide nuclei is ^{136}Xe(^{136}Xe,1n)^{271}Hs with the calculated cross section of 170 pb.

We obtain the cross section of 1.0 pb for ^{142}Ce(^{136}Xe,1n)^{277}112 (E_{lab} = 656.7 MeV). This means that the use of the heaviest stable isotope of cerium, ^{142}Ce, instead of magic ^{140}Ce, decreases the cross section by a factor of 2.9 (cf. Table 6).

>From our study, we draw the conclusion that the calculated cross section of the reaction ^{208}Pb(^{70}Zn,1n)^{277}112 is by a factor of 3.2 larger than that calculated for the symmetric reaction ^{142}Ce(^{136}Xe,1n)^{277}112 which may lead to the same nucleus. This conclusion is in sharp contrast to the suggestion made by the authors of Ref. [54] based on a very recent qualitative concept of "unshielded fusion" that the use of ^{142}Ce(^{136}Xe,1n)^{277}112 should give orders of magnitude better chance for producing ^{277}112 in comparison with the reaction ^{208}Pb(^{70}Zn,1n)^{277}112 carried out at GSI.

One should keep in mind, however, that heavy-ion fusion is far more complicated than a one-dimensional tunneling model suggests as it is known from subbarrier-fusion excitation-functions. For symmetric and nearly symmetric entrance channels, the c parameter may not necessarily be as good as for asymmetric channels. Whether one parameter c for all asymmetries in the entrance channel is a sufficiently broad cover for all the physics left out from the model, remains to be seen.

In the present paper, we introduced both more realistic fusion barrier and survival probability of the compound nucleus in comparison with our original model [28, 35, 49]. We reproduced the measured formation cross sections of transactinides and heavy actinides synthesized in reactions with the emission of only one neutron and indicated the most promising target-projectile-energy combinations for producing transactinide (superheavy) elements. Since our model depends on the input quantities, in particular on Q-value, neutron-separation energy S_n and fission-barrier height B_f for the compound nucleus, the use of different input quantities than those taken from Refs.[31, 32, 33] may change the results. An increase (decrease) of Q-value by 1 MeV increases (decreases) the formation cross section about $1.7-2.2$ times. An increase (decrease) of the height of the fission barrier by 0.5 MeV increases (decreases) usually the formation cross section by a factor of about $1.5-1.6$ while the same increase (decrease) of the neutron-separation energy decreases (increases) usually the cross section by a factor of about $1.2-1.3$. In the present study, the influence of vibrational excitations on the value of $(\Gamma_n/\Gamma_f)_l$ for spherical and transitional nuclei has not been taken into account. The collective enhancement factor k_{eq} for such nuclei may have a value from the range of 1 to 10 [37]. This in turn may increase the formation cross section for spherical and transitional nuclei listed in Table 4 (nuclei heavier than ^{282}114) and Table 5 by a factor of $1-10$.

1. S. Björnholm and W.J. Swiatecki, Nucl. Phys. **A391** (1982) 471.
2. R. Smolanczuk, Phys. Rev. **C63** (2001) 044607.

3. J. Blocki, Y. Boneh, J.R. Nix, J. Randrup, M. Robel, A.J. Sierk, and W.J. Swiatecki, Ann. of Phys. **113** (1978) 330.

4. B. Sikora, J. Bisplinghoff, M. Blann, W. Scobel, M. Beckerman, F. Plasil, R.L. Ferguson, J. Birkelund and W. Wilcke, Phys. Rev. **C25** (1982) 686.

5. J.R. Nix, and J. Sierk, Phys. Rev. **C21** (1980) 982.

6. W.D. Myers and W.J. Swiatecki, The macroscopic approach to nuclear masses and deformations, Lawrence Berkeley Laboratory preprints LBL-13929, 1982; Ann. Rev. Nucl. Part. Sci. **32** (1982) 309.

7. R. Bass, Nucl. Phys. **A231** (1974) 45.

8. M. Brack, J. Damgaard, A.S. Jensen, H.c. Pauli, V.M. Strutinskii, and C.Y. Wong, Rev. Mod. Phys. **44** (1972) 320.

9. F. Beck, J. Blocki and H. Feldmeier, Proc. Int. Workshop on gross properties of nuclei and nuclear excitations X, Hirschegg, Jan. 18-22, 1982.

10. J. Blocki and W.J. Swiatecki, Nuclear deformation energies, LBL-12811.

11. W.J. Swiatecki, Nucl. Phys. **A376** (1982) 275; W.J. Swiatecki, Proc. 4th Int. Conf. on nuclei far from stability, Helsinger, June 7-13, 1981, ed. P. G. Hansen.

12. H. Sann, R. Bock, T. Chu, A. Gobbi, A. Olmi, U. Lynen, W. Müller, S. Bjørnholm, and H. Esbensen, Phys. Rev. Lett. **47** (1981) 1248.

13. R. Bock, Y.T. Chu, M. Dakowski, A. Gobbi, E. Grosse, A. Olmi, H. Sann, D. Schwalm, U. Lynen. W. Müller, S. Bjørnholm, H. Esbensen, W. Wölfli and E. Morenzoni, Nucl. Phys. **A** (1982), to appear.

14. J.R. Huizenga, J.R. Birkelund, W.V. Schröder, W.W. Wilcke and H.J. Wollersheim, in Dynamics of heavy-ion collisions, ed. N. Cindro, R.A. Ricci and W. Greiner (North-Holland, Amsterdam, 1981) p. 15.

15. S. Cohen, F. Plasil and W.J. Swiatecki, Ann. of Phys. **82** (1974) 557.

16. W.J. Swiatecki, Proc. 4th Int. Conf. on nuclei far from stability, Helsinger, June 7-13, 1981, ed. P. G. Hansen.

17. G. Fai, Lawrence Berkeley Laboratory preprint LBL-14413, May 1982.

18. H. Gäggeler, W. Brüchle, J.V. Kratz, M. Schädel, K. Sümmerer, G. Wirth and T. Sikkeland, Proc. Int. Workshop on gross properties of nuclei and nuclear excitations X, Hirschegg, Jan. 18-22, 1982.

19. L.C. Vaz, J.M. Alexander and G.R. Satchler, Phys. Rep. **69** (1981) 373, Fig. 5.

20. G. Münzenberg, Rep. Prog. Phys. **51** (1988) 57 and references therein.

21. S. Hofmann, Rep. Prog. Phys. **61** (1998) 639 and references therein.

22. V. Ninov, K.E. Gregorich, W. Loveland, A. Ghiorso, D.C. Hoffman, D.M. Lee, H. Nitsche, W.J. Świątecki, U.W. Kirbach, C.A. Laue, J.L. Adams, J.B. Patin, D.A. Shaughnessy, D.A. Strellis, and P.A. Wilk, Phys. Rev. Lett. **83** (1999) 1104.

23. H.W. Gäggeler, D.T. Jost, A. Türler, P. Armbruster, W. Brüchle, H. Folger, F.P. Hessberger, S. Hofmann, G. Münzenberg, V. Ninov, W. Reisdorf, M. Schädel, K. Sümmerer, J.V. Kratz, U. Scherer, and M.E. Leino, Nucl. Phys. **A502** (1989)

561c.

24. H. Gauvin, Y. Le Beyec, M. Lefort, and C. Deprun, Phys. Rev. Lett. **28** (1972) 697.
25. C.Y. Wong, Phys. Lett. **42B** (1972) 186.
26. B. Nerlo-Pomorska and K. Pomorski, Z. Phys. **A348** (1994) 169..
27. R.W. Hasse and W.D. Myers, *Geometrical Relationships of Macroscopic Nuclear Physics* (Springer-Verlag, Berlin, 1988).
28. R. Smolańczuk, Phys. Rev. **C59**, 2634 (1999).
29. S. Hofmann, V. Ninov, F.P. Hessberger, P. Armbruster, H. Folger, G. Münzenberg, H.J. Schött, A.G. Popeko, A.V. Yeremin, A.N. Andreyev, S. Saro, R. Janik, and M. Leino, Z. Phys. **A350** (1995) 277.
30. W.E. Parker, M. Kaplan, D.J. Moses, G. La Rana, D. Logan, R. Lacey, J.M. Alexander, D.M. de Castro Rizzo, P. DeYoung, R.J. Welberry, and J.T. Boger, Phys. Rev. C **44** (1991) 774.
31. R. Smolańczuk, Phys. Rev. **C56** (1997) 812.
32. R. Smolańczuk, Ph.D. thesis, Soltan Institute for Nuclear Studies, Warsaw, 1996.
33. R. Smolańczuk, J. Skalski, and A. Sobiczewski, Phys. Rev. **C52** (1995) 1871.
34. A.N. Andreyev, D.D. Bogdanov, V.I. Chepigin, A.P. Kabachenko, O.N. Malyshev, Yu.Ts. Oganessian, A.G. Popeko, J. Roháč, R.N. Sagaidak, A.V. Taranenko, G.M. Ter-Akopian, and A.V. Yeremin, Preprint JINR E7-94-378, Dubna, 1994; in *Proceedings of the Workshop on Heavy-Ion Fusion: Exploring the Variety of Nuclear Properties*, Padova, Italy, 1994 (World Scientific, Singapore, 1994), p.260.
35. R. Smolańczuk, Phys. Rev. Lett. **83** (1999) 4705.
36. S. Bjornholm, A. Bohr, and B.R. Mottelson, *in Proceedings of the Symposium on Physics and Chemistry of Fission*, Rochester, 1973 (IAEA, Vienna, 1974), Vol. 1, p. 367.
37. A.R. Junghans, M. de Jong, H.-G. Clerc, A.V. Ignatyuk, G.A. Kudyaev, and K.-H. Schmidt, Nucl. Phys. **A629** (1998) 635.
38. B. Vandenbosch and J.R. Huizenga, *Nuclear Fission* (Academic, New York, 1973).
39. V.E. Viola, Jr. and B.D. Wilkins, Nucl. Phys. **82** (1966) 65.
40. H. Hagelund and A.S. Jensen, Phys. Scr. **15** (1977) 225.
41. A. Gilbert and A. Cameron, Can. J. Phys. **43**, 1446 (1965).
42. G. Audi, O. Bersillon, J. Blachot, and A.H. Wapstra, Nucl. Phys. **A624**, 1 (1997).
43. F.P. Hessberger, G. Münzenberg, S. Hofmann, W. Reisdorf, K.H. Schmidt, H.J. Schött, P. Armbruster, R. Hingmann, B. Thuma, and D. Vermeulen, Z. Phys. **A321** (1985) 317.
44. G. Münzenberg, S. Hofmann, H. Folger, F.P. Hessberger, J. Keller, K. Poppensieker, B. Quint, W. Reisdorf, K.-H. Schmidt, H.J. Schött, P. Armbruster, M.E. Leino, and R. Hingmann, Z. Phys. **A322** (1985) 227.
45. G. Münzenberg, P. Armbruster, G. Berthes, H. Folger, F.P. Hessberger, S. Hof-

mann, J. Keller, K. Poppensieker, A.B. Quint, W. Reisdorf, K.H. Schmidt, H.J. Schött, K. Sümmerer, I. Zychor, M.E. Leino, R. Hingmann, U. Gollerthan, and E. Hanelt, Z. Phys. **A328** (1987) 49.

46. C.C. Sahm, H.-G. Clerc, K.-H. Schmidt, W. Reisdorf, P. Armbruster, F.P. Hessberger, J.G. Keller, G. Münzenberg and D. Vermeulen, Nucl. Phys. **A441** (1985) 316.
47. J.G. Keller, K.-H. Schmidt, F.P. Hessberger, G. Münzenberg, W. Reisdorf, H.G. Clerc, and C.-C. Sahm, Nucl. Phys. **A452** (1986) 173.
48. G.G. Adamian, N.V. Antonenko, and W. Scheid, Nucl. Phys. **A678** (2000) 24.
49. R. Smolańczuk, Phys. Rev. **C61** (2000) 011601.
50. R. Smolańczuk, Phys. Rev. **C60** (1999) 021301.
51. S. Ćwiok, W. Nazarewicz, and P.H. Heenen, Phys. Rev. Lett. **83** (1999) 1108.
52. M. Bender, Phys. Rev. C **61** (2000) 031302.
53. Yu.A. Lazarev, Yu.V. Lobanov, Yu.Ts. Oganessian, V.K. Utyonkov, F.Sh. Abdullin, A.N. Polyakov, J. Rigol, I.V. Shirokovsky, Yu.S. Tsyganov, S. Iliev, V.G. Subbotin, A.M. Sukhov, G.V. Buklanov, B.N. Gikal, V.B. Kutner, A.N. Mezentsev, K. Subotic, J.F. Wild, R.W. Lougheed and K.J. Moody, Phys. Rev. C **54**, 620 (1996).
54. W.D. Myers and W.J. Świątecki, Phys. Rev. C **62**, 044610 (2000).